

From cold to hot irradiated gaseous exoplanets: Fingerprints of chemical disequilibrium in atmospheric spectra

KARAN MOLAVERDIKHANI,¹ THOMAS HENNING,¹ AND PAUL MOLLIERE²

¹*Max Planck Institute for Astronomy, Königstuhl 17, 69117 Heidelberg, Germany*

²*Sterrewacht Leiden, Huygens Laboratory, Niels Bohrweg 2, 2333 CA Leiden, The Netherlands*

(Received TBD; Revised TBD; Accepted TBD)

ABSTRACT

Almost all planetary atmospheres are affected by disequilibrium chemical processes. In this paper we introduce our recently developed Chemical Kinetic Model (**ChemKM**). We show that the results of our HD 189733b model are in good agreement with previously published results, except at μ bar regime, where molecular diffusion and photochemistry are the dominant processes. We thus recommend careful consideration of these processes when abundances at the top of the atmosphere are desired. We also propose a new metric for a quantitative measure of quenching levels. By applying this metric, we find that quenching pressure decreases with the effective temperature of planets, but it also varies significantly with other atmospheric parameters such as [Fe/H], $\log(g)$, and C/O. In addition, we find that the “Methane Valley”, a region between 800 and 1500 K where above a certain C/O threshold value a greater chance of CH₄ detection is expected, still exists after including the vertical mixing. The first robust CH₄ detection on an irradiated planet (HD 102195b) places this object within this region; supporting our prediction. We also investigate the detectability of disequilibrium spectral fingerprints by JWST, and suggest focusing on the targets with T_{eff} between 1000 and 1800 K, orbiting around M-dwarfs, having low surface gravity but high metallicity and a C/O ratio value around unity. Finally, constructing Spitzer color-maps suggests that the main two color-populations are largely insensitive to the vertical mixing. Therefore any deviation of observational points from these populations are likely due to the presence of clouds and not disequilibrium processes. However, some cold planets ($T_{\text{eff}} < 900$ K) with very low C/O ratios (< 0.25) show significant deviations; making these planets interesting cases for further investigation.

Keywords: planets and satellites: atmospheres — planets and satellites: composition — methods: numerical

1. INTRODUCTION

The atmospheric composition of solar system planets is not at their thermochemical equilibrium state, mostly due to the irradiation by the Sun and mixing through atmospheric transport and turbulence. These effects are so pronounced that even the earliest atmospheric models of these objects include disequilibrium chemistry (e.g. review articles on the early modern models of Venus (Noll & McElroy 1972), Earth (Lou 1973), Mars (Noll & McElroy 1974), Jupiter (Danielson 1968), Saturn (Divine 1972), Titan (Divine 1974), Uranus, and Neptune (Encrenaz 1974)).

With the discovery of Hot Jupiters (Mayor & Queloz 1995), however, the assumption of thermochemical equilibrium resurfaced as a first-order estimation of their atmospheric properties thanks to their high temperatures (e.g. Burrows & Sharp 1999; Lodders & Fegley 2002; Fortney et al. 2005). But further studies suggested that the non-thermal processes could potentially alter their chemical composition at the photospheric levels; predominantly because of the intense UV irradiation and strong atmospheric mixing (e.g. Seager et al. 2005; Madhusudhan & Seager 2009; Stevenson et al. 2010; Moses et al. 2011; Agúndez et al. 2012; Venot et al. 2012; Hu et al. 2012, 2013; Hébrard et al. 2013; Hu & Seager 2014; Miguel et al. 2014; Zahnle & Marley 2014; Drummond et al. 2016; Tsai et al. 2017; Wang et al. 2017; Blumenthal et al. 2018; Zhang & Showman 2018; Changeat

et al. 2019) or other processes such as lightning (Helling & Rimmer 2019) and cosmic rays (Rimmer & Helling 2013).

Madhusudhan & Seager (2011) performed an extensive retrieval analysis of the GJ 436b spectrum observed by Stevenson et al. (2010) and concluded that the methane abundance paucity cannot be explained by thermoequilibrium chemistry. While the lack of a robust methane detection in the spectra of irradiated gaseous planets (e.g. Brogi et al. 2016, 2018; Pino et al. 2018; Alonso-Floriano et al. 2019) could be an indication of disequilibrium chemistry, there is no large-scale systematic investigation of how disequilibrium processes change the abundance of methane (or any other major opacity compound) at photospheric pressures (~ 1 bar to $\sim 1 \mu\text{bar}$), and how this manifests itself in the atmospheric spectra. Zahnle & Marley (2014) and Miguel & Kaltenecker (2014) both perform such studies however over a limited parameter space. The complexity of photochemical models makes the large-scale simulations computationally expensive, and thus such investigations require code optimization. In addition, the models must be flexible and generic enough to perform efficiently over a range of atmospheric conditions and compositions.

We introduce a new chemical kinetic model (**ChemKM**), which is both fast and generic. We employ **ChemKM** to perform an extensive parameter study over a broad range of atmospheric conditions. In total, we calculate 84,672 full-network chemical kinetic models with more than 100 reactants and 1000 reactions, to study how the variation of major opacity sources (e.g. H_2O , CH_4 , CO , and CO_2) due to disequilibrium chemistry affect the spectra. We also present a case study of HD 189733b, a well-studied exoplanet, for benchmarking.

In what follows, we describe our chemical kinetic model and the parameter space that we have explored. In Section 3.1, we present the results of our case study for HD 189733b and benchmark it against the model developed by Venot (2012). In the rest of Section 3, we present the results of our parametric study and check the validity of our proposed classification scheme for irradiated planetary spectra (see Molaverdikhani et al. (2019) for more details on the classification under cloud-free equilibrium chemistry conditions). In Section 3.3, we report the dependency of quenching point on atmospheric parameters, and in Section 3.4 we investigate the detectability of disequilibrium processes by JWST. Finally, in Section 3.5 we discuss Spitzer transmission and emission color diagrams variation from thermochemical equilibrium models due to the vertical mixing, and its observability. We summarize and conclude our results and findings in Section 4.

2. METHODS

2.1. *ChemKM: The Chemical Kinetic Model*

To study the effects of disequilibrium chemistry on the composition and atmospheric spectra of irradiated exoplanets we developed a 1D Chemical Kinetic Model (**ChemKM**). The abundances of atmospheric constituents are governed by numerically solving the equations of chemical kinetics (also known as the altitude-dependent continuity–diffusion equation) which describe the formation and destruction of species, equation 1 (e.g. Allen et al. 1981):

$$\frac{\partial n_i}{\partial t} = P_i - L_i - \frac{\partial \Phi_i}{\partial z}, \quad (1)$$

where n_i is the number density (cm^{-3}), P_i is the chemical production rate ($\text{cm}^{-3} \text{s}^{-1}$), L_i is the chemical loss rate ($\text{cm}^{-3} \text{s}^{-1}$), and Φ_i is the net vertical flux ($\text{cm}^{-2} \text{s}^{-1}$) of species i at altitude z . These quantities are all functions of time t and altitude z (or alternatively pressure). The vertical flux transport terms include molecular and eddy diffusion, $\Phi_i = \Phi_{i,mol} + \Phi_{i,eddy}$ where the latter is commonly parameterized by an eddy diffusion coefficient K_{zz} . The vertical flux transport terms can be estimated through equations 2 and 3, respectively (see e.g. Moses (1991) and references therein).

$$\Phi_{i,mol} = -n_T D_i \left(\frac{\partial f_i}{\partial z} - \frac{f_i}{H_a} + \frac{f_i}{H_i} + \frac{\alpha_i f_i}{T} \frac{dT}{dz} \right) \quad (2)$$

$$\Phi_{i,eddy} = -n_T K_{zz} \left(\frac{\partial f_i}{\partial z} \right), \quad (3)$$

where K_{zz} is the eddy diffusion coefficient ($\text{cm}^2 \text{s}^{-1}$), D_i is the molecular diffusion coefficient ($\text{cm}^2 \text{s}^{-1}$), n_T is the total number density, f_i is the mixing ratio of species i and is defined as $f_i = n_i/n_T$, H_a is the mean scale height of the atmosphere, H_i is the scale height of species i , T is the temperature (K), and α_i is the thermal diffusion factor of species i .

We use Lennard-Jones calculations for the estimation of molecular diffusivity of species. An updated list of Lennard-Jones potentials can be obtained from Appendix-B of Poling et al. (2000). Note that D_i scales inversely with pressure and will become important at very low pressures. Therefore this term's contribution is no longer negligible at the pressures probed by transmission observations, i.e. above ~ 1 bar. The effect becomes more pronounced when the atmosphere is probed by high resolution spectroscopy. We discuss this in more detail in Section 3.1.

One approach to estimate K_{zz} is using general circulation models (GCMs) to calculate wind velocity fields

(e.g. Moses et al. (2011)) or to compute the advection of passive tracers (Parmentier et al. 2013). Due to large uncertainties in these approaches an alternative method could be to treat the eddy diffusion coefficient as a free parameter in the model (e.g. Miguel & Kaltenegger 2014). We use the latter approach, in our parametric study.

For an overview of our methodology, numerical solution, and chemical networks see Appendix A. In Appendix B, we present the results of verification of our model under different conditions such as thermochemical equilibrium or by including molecular and eddy diffusion, photochemistry, condensation, and setting up atmospheric influxes and different boundary conditions.

2.2. The temperature structures for the parametric study

In Section 3, we study a broad range of parameter space, based on a large grid of cloud-free atmospheric models. We use the self-consistently calculated temperature-abundances profiles as the input of our chemical kinetic model (ChemKM) to calculate the effect of vertical mixing on the chemical composition of the atmospheres. The input profiles were calculated by the petitCODE (Mollière et al. 2015, 2017). We then use petitRADTRANS to calculate the spectra of atmospheres at chemical disequilibrium to investigate how the quenching point changes with atmospheric parameters, and whether the classification scheme proposed in (Molaverdikhani et al. 2019) would still hold after introducing vertical mixing. Here we briefly review the properties of the grid and the range of investigated parameters.

In the first paper of this series (Molaverdikhani et al. 2019) we calculated a large grid of 28,224 self-consistent cloud-free atmospheric models using the petitCODE. The petitCODE is able to calculate planetary atmospheric temperature profiles, chemical abundances, and emergent and transmission spectra and it assumes radiative-convective and thermochemical equilibrium in a 1D setup. The stellar effective temperature, stellar radius, planetary effective temperature or distance, planetary internal temperature, planetary radius, planetary mass or alternatively its surface gravity and irradiation treatment must be provided.

We considered five factors as the free parameters in our petitCODE grid models: planetary effective temperature (T_{eff}), surface gravity ($\log(g)$), metallicity ($[\text{Fe}/\text{H}]$), carbon-to-oxygen ratio (C/O) and spectral type of the host star. The lower limit of T_{eff} was set to 400 K to avoid non-negligible contributions of the interior temperature (all models have $T_{\text{int}} = 200$ K) into

the atmospheric properties, and the upper limit was chosen to be 2600 K to avoid highly irradiated regions where the heat redistribution becomes inefficient and the planetary average irradiation treatment might become invalid. The surface gravity spans from 2.0 to 5.0 to broadly cover possible surface gravity values. Metallicity ranges from -1.0 to 2.0 with an increment of 0.5. The stellar spectral types were chosen to be M5, K5, G5 and F5. For C/O we selected irregular parameter steps ranging from 0.25 to 1.25 with smaller steps around unity to capture possible transitions from water- to methane-dominated atmospheres as predicted by Madhusudhan (2012), reported by Mollière et al. (2015), and discussed in detail in Molaverdikhani et al. (2019). We then add K_{zz} as a new dimension to be explored; more discussion and results in Section 3. Planetary spectra are calculated with petitRADTRANS (Mollière et al. 2019).

3. RESULTS

3.1. Case study: HD 189733b

HD 189733b is one of the most studied exoplanets so far (e.g. Moses et al. 2011) and hence represent a proper case for benchmarking. Moses et al. (2011) provided the thermal structure and the K_{zz} profile for this planet, which has been used by several studies to perform benchmark calculations (e.g. Venot et al. 2012; Moses 2014; Drummond et al. 2016; Tsai et al. 2017). Thus we use the same set of inputs to compare the outcome of our HD 189733b model with previously published results.

To set up the model, we use Venot et al. (2012)'s full kinetic network and an updated version of Hébrard et al. (2012)'s UV absorption cross-sections and branching yields. For UV irradiation at TOA, both Moses et al. (2011) and Venot et al. (2012) used ϵ Eridani as a proxy of HD 189733 due to their similarities in spectral type, age, and metallicity. Lack of high quality data at shorter wavelengths led them to use only a portion of ϵ Eridani's spectrum (Moses et al. (2011) used ϵ Eridani's data in the range of 115 nm to 283 nm and Venot et al. (2012) uses data between 90 nm and 330 nm). They combined other datasets and models to extend the spectrum. We use the most recent measurements of ϵ Eridani as a full and coherent spectrum from X-ray to optical to take a more consistent approach. The data were obtained from the MUSCLES database (France et al. 2016). We initialize the atmospheric composition at its thermochemical equilibrium state and let the model reach its steady state after an integration time of 10^9 sec.

Venot et al. (2012) and Moses (2014) reported the importance of kinetic network and its effect on the quenching level and quenching abundances. Since we opted for the usage of Venot et al. (2012)'s network, we com-

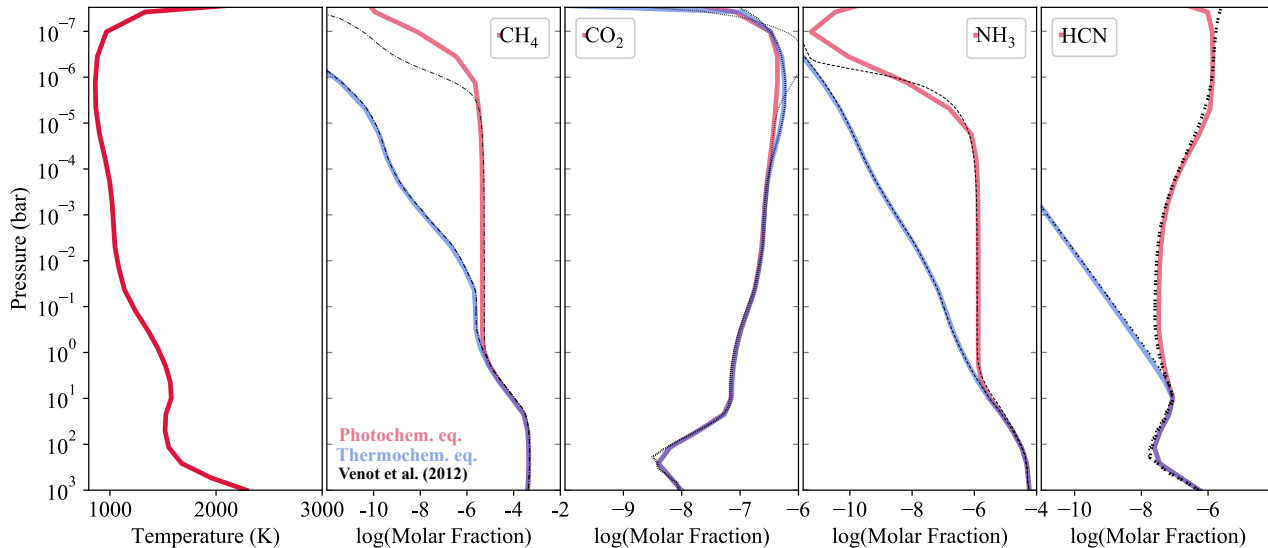


Figure 1. HD 189733b photochemical model comparison. **Left)** The temperature structure. **Rest of panels)** ChemKM’s calculated abundances of CH_4 , CO_2 , NH_3 , HCN , and H at thermochemical equilibrium (solid blue lines) and photo-diffusion equilibrium (solid red lines), compared with the results of Venot et al. (2012) (black lines). The results are in good agreement except at and above the μbar regime, where photolysis reactions and molecular diffusion are the dominant processes. Hence a careful implementation of these processes is necessary if TOA abundances are desired.

pare our results with their findings. Our thermochemical equilibrium abundances (blue lines in Figure 1) are almost identical to the Venot et al. (2012)’s results. Similarly, our disequilibrium abundances (red lines in Figure 1) are almost identical, except in the μbar regime. By using the same stellar flux as Venot et al. (2012) and finding no significant abundance variation, we rule out the role of stellar flux as a cause of discrepancies at high altitudes. Therefore, these subtle differences between HD 189733b photochemical models are likely caused by different molecular diffusion implementation and different photolysis reactions. As briefly mentioned in Section 2.1, this might have significant consequences in the interpretation of high-resolution spectra.

3.2. Methane depletion in GJ 436b

We discussed that while the atmospheric composition of deeper regions of gaseous planets tend to remain at thermochemical equilibrium, their photospheres are usually prone to disequilibrium processes. This effect may have its fingerprint on the planets’ atmospheric spectra, but its detection is not a trivial task with the current observational facilities.

In a well-known case, Stevenson et al. (2010) reported CH_4 depletion inferred from the thermal emission of the GJ 436b dayside (a Class-I planet with $T \sim 700$ K). Several studies suggested that this CH_4 deficiency, relative to its thermochemical equilibrium predictions, could be explained by disequilibrium processes such as diffusion and polymerization of CH_4 (see e.g. Stevenson

et al. 2010; Madhusudhan & Seager 2011; Line et al. 2011). Madhusudhan & Seager (2011) performed a detailed retrieval analysis of the spectrum and concluded that the atmosphere maintains a possible high metallicity ($10\times$ solar) and a vertical mixing with $K_{zz} \approx 10^6 - 10^7$ ($\text{cm}^2 \text{ s}^{-1}$). They constrained these values by assuming a suite of parametric TP structures. Under thermochemical equilibrium conditions, such temperature profiles could result in a monotonically decreasing CH_4 abundance at the upper portion of the atmosphere. If the mixing timescale is much shorter than the kinetic timescales at those pressures, then the vertical mixing could “transport” these deeper/lower abundances and bring them to the upper levels. Hence a CH_4 deficiency at TOA could occur under these conditions. Such abundance variation could change the measured flux by *Spitzer* IRAC instrument in particular the $3.6 \mu\text{m}$ channel (Stevenson et al. 2010).

To illustrate how such an abundance deficiency occurs, we setup a simple model by selecting a parametric TP structure from Madhusudhan & Seager (2011), Figure 2 (a). Here, we do not intend to perform a retrieval to reproduce the Madhusudhan & Seager (2011)’s results, but rather it is a demonstration of abundance variation at TOA due to imposing the vertical mixing. We assume 500 K and 1500 K for the temperature of upper and deeper regions respectively, with solar metallicity and C/O ratio for the bulk composition of the atmosphere. With this setup, methane’s thermochemical equilibrium abundance at TOA is around 4.6×10^{-4} . By increasing

the vertical mixing, the atmosphere quenches at deeper levels, see Figure 2 (b). The CH₄ abundance at TOA decreases as K_{zz} increases, as long as quenching occurs at pressures smaller than ~1 bar. Any K_{zz} higher than 10⁵ cm² s⁻¹, however, mixes the deeper levels where CH₄ has higher abundances; causing to an enhancement of CH₄ abundance at TOA. Figure 2 (c) illustrates the variation of CH₄ at TOA, due to the change of vertical mixing, and a minimum CH₄ abundance in the case of K_{zz}=10⁵ cm² s⁻¹. Here we only showed the results of CH₄ abundance, however, almost all reagents respond to the variation of vertical diffusion; although differently. Their collective variation could affect the transmission spectrum of the planet as can be seen in Figure 2 (d).

This non-linear atmospheric response is likely to be more pronounced for hotter planets, e.g. Class-II, where the abundance of methane and water (as two of the major opacity sources in the planetary atmospheres) are more sensitive to the variation of C/O ratio at their photospheres due to partial evaporation of condensates.

We expand these results by conducting an extensive survey on the effect of vertical mixing in the spectra of our self-consistently calculated cloud-free grid of models (see Section 2.2 and (Molaverdikhani et al. 2019)). By using these TP structures as ChemKM's input and assuming three values for K_{zz} (10⁶, 10⁹, and 10¹² cm² s⁻¹) we calculate the atmospheric abundances of these planets at their diffusion equilibrium. The grid of models and their emission and transmission spectra will be publicly available.¹ As the first step, we determine the dependency of quenching levels to the atmospheric parameters.

3.3. Parametric study: Quenching levels

The atmospheric diffusion not always results in a constant "quenched abundance" above the "quenching level" (see, e.g., Figure 15, and Section B.3 for an overview). Therefore, this definition of quenching level (and consequently constant quenched abundance) is not general. Here we propose a parameter, the Coefficient of variation (CV), for a quantitative definition of quenching levels based on the deviation of abundances from their thermochemical equilibrium values at each pressure level.

This parameter is a standardized measure of dispersion of a quantity and has been used in other fields, e.g. in the clinical research (Schiff et al. 2014), to estimate deviation of particular quantities from its mean value. In this work, we introduce this parameter as a mean to quantitatively estimate the quenching levels. In the chemical kinetic simulations, this parameter can

be calculated as the ratio of the temporal standard deviation of abundances, s , to the mean value of abundances for a given species at any given pressure level. In our simulations, we use exponential time steps to calculate abundances, hence a better parameter would be the geometric Coefficient of variation (gCV) of abundances. This can be calculated as follows:

$$\text{gCV} = \sqrt{e^{s_{\ln}^2} - 1}, \quad (4)$$

where s_{\ln} is the sample standard deviation of abundances after a natural log transformation and can be estimated as $s_{\ln} = s \ln(10)$. Stronger variation of abundance at any given altitude results in a higher gCV. We find that $\text{gCV}_i = 0.05$ represents the onset of disequilibrium chemistry of species i very well, hence $\text{gCV}_i \geq 0.05$ can be used to mark the regions at which abundances have deviated from their thermochemical equilibrium values significantly. An example is given in Figure 3 based on the results of our diffusion verification model (presented in Figure 15), where water remains in thermochemical equilibrium when $\text{gCV}_{\text{H}_2\text{O}} < 0.05$ (below the red dash-dotted line at ~0.5 mbar) and is driven away from it when $\text{gCV}_{\text{H}_2\text{O}} \geq 0.05$ (above ~0.5 mbar). The bottom panel in Figure 3 shows the temporal evolution of abundances at different pressures. At the times longer than $t > 10^{11}$ sec, abundances reach to steady state at all pressures.

We present the results based on the "quench point from each species", gCV_i . An alternative method would be to calculate all the timescales relevant for a species at any given pressure. While the alternative method is mathematically correct, our method provides a much simpler picture of the quenching levels based on the actual abundance variation due to the kinetics. Another advantage of our method is that there is no need to trace all the reactions and timescales when calculating the abundances, and the quenching can easily be calculated once the simulations are over. The gCV can be also used in a broader sense to study any abundance deviation from any initial condition as a standard mathematical method for such analysis.

By using this new metric we investigate the quenching levels in our grid of models. Figure 4 (a) shows the density plot of quenching levels of all species in our K_{zz}=10¹² cm² s⁻¹ models. In general, P_{quench} decreases to lower pressures as temperature increases, but its variation at any given temperature is large. For instance, models with T_{eff}=2600 K have shown quenching at all pressures ranging from 100 to 10⁻⁸bar in these simulations. But, if we calculate the average P_{quench} along T_{eff} (solid black line) the result is similar to the Venot et al.

¹ www.mpia.de/homes/karan

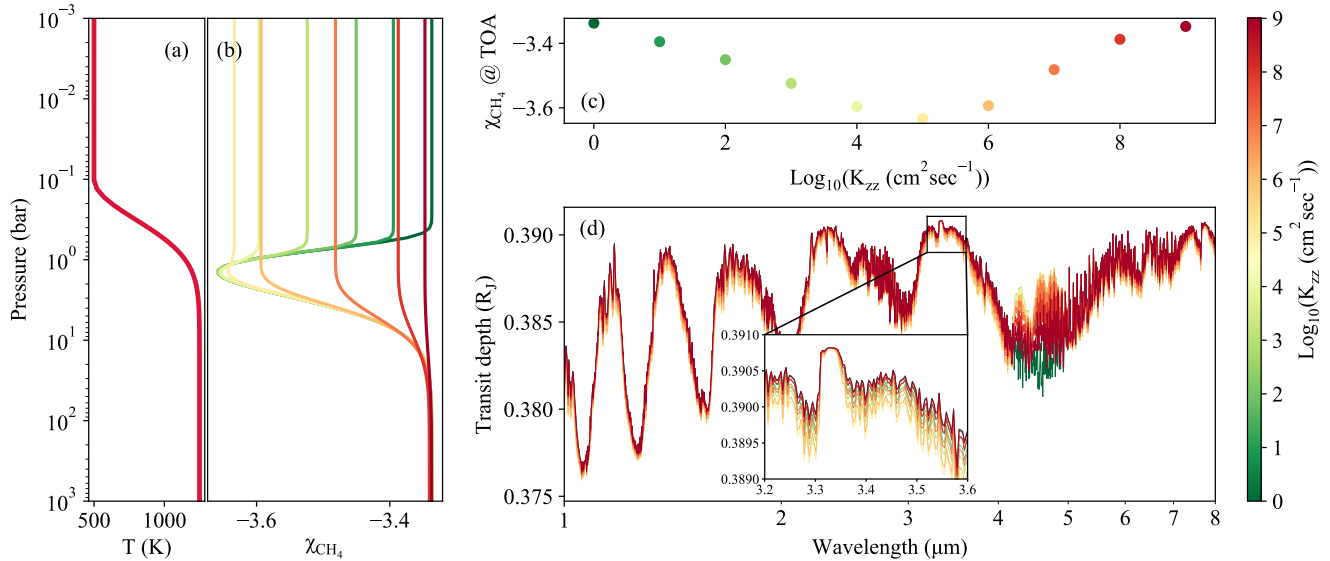


Figure 2. Effect of vertical mixing on CH₄ abundances at the top of the atmosphere. (a) A simple parametric GJ 436b–like TP structure, adapted from Madhusudhan & Seager (2011). (b) CH₄ abundance profiles caused by different K_{zz} values. Stronger mixing causes a deeper quenching level, but does not guarantee a monotonic abundance variation. (c) CH₄ abundance at TOA as a function of K_{zz} in this particular case. (d) Variation of the transmission spectrum as a function of K_{zz}. In this example, variation of CH₄ abundance at TOA appears as a slight shift in the transmission spectrum. The CO₂ and CO spectral features, between 4–5 μm, varies as well; resulting in higher CO₂ and CO molar fractions at TOA when the mixing is in action.

(2018) results of P_{quench} for $K_{zz}=10^{12} \text{ cm}^2 \text{ s}^{-1}$, dashed line in Figure 4 (a).

We find that for a given mixing strength, quenching levels strongly depend on the effective temperature of the planet, but it also depends on the complexity of abundance profiles. For instance, in most cases if a species is the dominant species, then its abundance profile tends to be almost constant. This constant shape of the profiles leads to an underestimation of their P_{quench} (their abundance does not change very much by mixing since it is constant already, therefore gCV_i remains small at higher pressures and a lower P_{quench} will be determined). This “constant profiles” region is marked by a dotted line in Figure 4.

The role of T_{eff} (and K_{zz}) on the determination of P_{quench} is rather obvious by following the chemical versus mixing timescale argument; e.g. see Section B.3. However, relating atmospheric parameters to the complexity of abundance profiles is not trivial. Nevertheless, we find that all atmospheric parameters that we have investigated (i.e. T_{eff} , $\log(g)$, $[\text{Fe}/\text{H}]$, and C/O) affect the complexity of abundance profiles up to some degree. The averaged value of $[\text{Fe}/\text{H}]$, $\log(g)$, and C/O (calculated in each 2D histogram bin represented in the panel (a) of Figure 4) are shown in Figure 4 panels (b), (c), and (d) respectively, to present a graphical demonstration of these dependencies. While Venot et al. (2018) also explored the effect of C/O ratio on the quenching levels, they only found negligible variation. This

is mainly due to their narrower parameter-space coverage and their methodology for the determination of the quenching levels as an integrated quantity over the main species.

We will use gCV_i to present an empirical equation for $P_{\text{quench}}([\text{Fe}/\text{H}], \log(g), \text{C}/\text{O})$ in a follow-up paper.

3.4. Observability of the disequilibrium chemistry with JWST

One of the key upcoming missions to address the diversity and characterization of exoplanetary atmospheres is JWST. Naturally, the first question would be: “Is there any sweet-spot in the parameter-space to detect the effect of disequilibrium chemistry in the planetary spectra by JWST?”. In order to investigate this, we take a simple approach by subtracting the transmission spectra of each atmospheric model at thermochemical equilibrium and disequilibrium chemistry. The wavelength range spans 0.8 μm to 20 μm, covering most of the JWST’s wavelength range. The shorter wavelengths, i.e. 0.6 μm to 0.8 μm, would be likely influenced by the Rayleigh scattering and wavelengths longer than 20 μm do not show significant molecular features; hence excluded from this analysis. We then find the maximum spectral deviation for each model due to the disequilibrium.

We should, however, note that using the measured radius at one wavelength is not adequate for a robust detection of disequilibrium fingerprint on the spectra

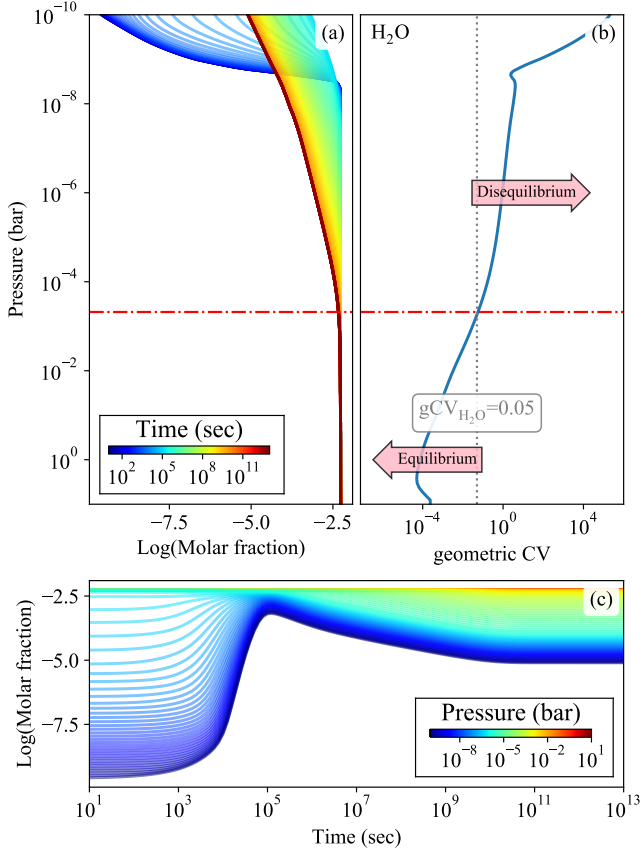


Figure 3. A quantitative definition of disequilibrium. We use the results of our diffusion verification model (presented in Figure 15) as an example. (a) Temporal variation of H₂O abundance from thermochemical equilibrium (blue) to diffusion equilibrium (red). (b) Water remains in thermochemical equilibrium when $gCV_{H_2O} < 0.05$ (below the red dash-dotted line at ~ 0.5 mbar) and is driven away from the thermochemical equilibrium when $gCV_{H_2O} \geq 0.05$ (above ~ 0.5 mbar). The red dash-dotted line marks the quenching point. (c) Temporal evolution of water abundances at different pressures. Invariant abundances at $t > 10^{11}$ sec insures diffusion equilibrium.

due to the reference pressure degeneracy. Therefore, this analysis should be taken only as a first step toward a spectrum-sensitivity analysis and not a retrieval-degeneracy analysis.

Figure 5 shows an example of the transmission spectra for a Jupiter-sized planet around a G5-type star, with solar metallicity, $C/O \sim 0.5$, and a surface gravity of 3.5 under two conditions: the thermochemical equilibrium and diffusion equilibrium. The diffusion equilibrium model is shown for $K_{zz} = 10^{12} \text{ cm}^2 \text{ s}^{-1}$. In this example, the maximum difference between the spectra of the two models, ΔTD , occurs at the CH₄ feature at $\sim 3.3 \mu\text{m}$. The difference is about 150 ppm in this model; see the bottom panel of the same figure. While this CH₄

spectral feature is one of the most prominent features to detect the fingerprints of disequilibrium chemistry, other spectral features from CH₄, H₂O, CO₂, or CO could be also used as the disequilibrium tracing features. To produce Figure 6, we analyzed where in a spectrum the ΔTD was maximal for all spectra in the grid and calculated the occurrence at different wavelengths. By finding these occurrence rates we determine which wavelengths are likely to have the highest sensitivity to the vertical mixing. We identify five spectral regions with the highest occurrence rates at $\sim 1 \mu\text{m}$ (CH₄, H₂O, or CO), $\sim 3.3 \mu\text{m}$ (mostly CH₄), $\sim 4.5 \mu\text{m}$ (CO₂ or CO), $\sim 12 \mu\text{m}$ (CH₄), and $\sim 15 \mu\text{m}$ (CH₄). Hence, investigation of these wavelengths could provide a higher chance of the detection of disequilibrium spectral signature.

Blumenthal et al. (2018) performed a case study comparing the synthetic emission spectra of HD 189733b, WASP-80b, and GJ 436b. They found that the most significant differences in the emission spectra of these planets within the wavelength range of 4 to 5 μm are due to CO₂ and CO disequilibrium processes. Although our predictions are based on the synthetic transmission spectra, their results are consistent with our findings for the mentioned wavelength range; see Figure 6.

By averaging the maximum ΔTD over the free parameters domain, i.e. T_{eff} , $\log(g)$, $[Fe/H]$, C/O ratio, and the spectral type of the star (or alternatively its surface temperature, i.e. T_{star}), we identify the parameter-space at which the transmission spectra are highly sensitive to the vertical mixing. The results are shown in Figure 7. The $T_{\text{eff}}-\log(g)$ panel, at the top-left, suggests a strong dependency of disequilibrium detectability on the surface gravity of the planet. While this is not surprising, this panel shows a higher probability of disequilibrium detection at T_{eff} between 1000 and 2000 K. This region coincides with the Class-II and Class-III planets, where the evaporation of condensates plays a crucial role in the photospheric chemistry of planets. In fact, all T_{eff} -dependent results in the left column support this finding. Moreover, the $T_{\text{eff}}-C/O$ panel reveals an interesting trend: as T_{eff} increases, a higher chance of disequilibrium detectability occurs at higher C/O ratios. More precisely, there is a region around $C/O \sim 0.95$ with a higher probability of disequilibrium detection. This coincides with the minimum-IR opacity/inversion temperature profiles (see e.g. Mollière et al. 2015). It appears that such atmospheric condition makes the chemistry to be more easily driven away from its thermochemical equilibrium state. Therefore, this feedback could make the inversion due the minimum-IR opacity, chemically and radiatively unstable. A further self-consistent disequilibrium chemistry calculation must be performed

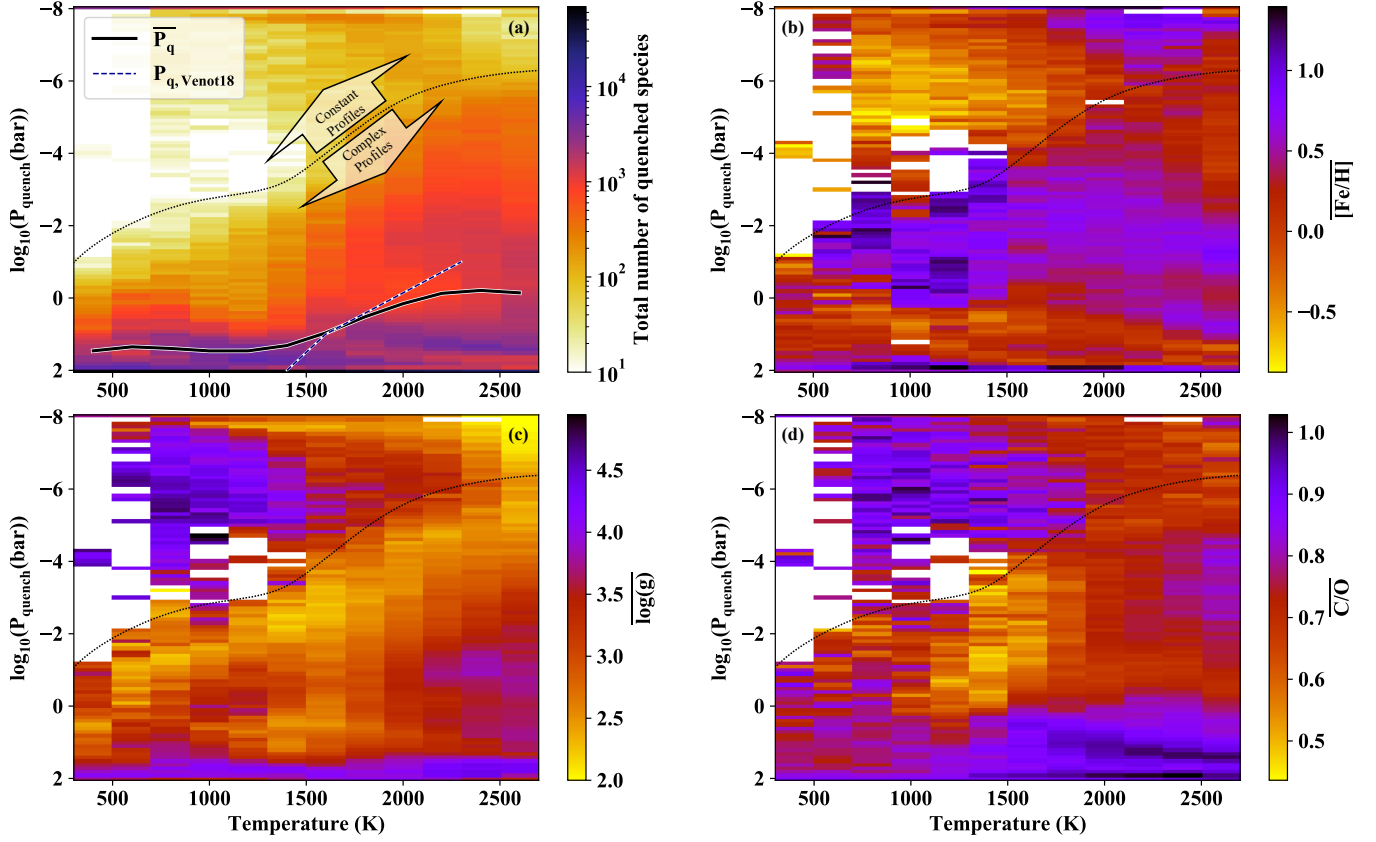


Figure 4. A quantitative determination of quenching levels in our grid of chemical kinetic models for $K_{zz}=10^{12} \text{ cm}^2 \text{ s}^{-1}$ cases. (a) Density plot of quenching levels of all species. In general, P_{quench} decreases to lower pressures as temperature increases, but its variation at any given temperature is large. However, the average P_{quench} (solid black line) is similar to the Venot et al. (2018) results of P_{quench} for $K_{zz}=10^{12} \text{ cm}^2 \text{ s}^{-1}$, dashed line. Constant abundance profiles of abundant species cause estimation of P_{quench} at lower pressures (above dotted line). (b,c,d) Maps of average [Fe/H], $\log(g)$, and C/O to graphically demonstrate P_{quench} degree of dependence to these parameters.

in order to quantitatively assess the significance of this feedback on the inversion.

The T_{star} -dependent panels, bottom row in Figure 7, illustrate a higher probability of disequilibrium detection when the host stars are colder. This is solely due to the fact that colder stars are associated with smaller radius; hence a larger transit depth for a given planetary radius. The $T_{\text{star}}-\log(g)$ panel also suggests that the detection of disequilibrium for a Jupiter-sized planet with high surface gravity maybe only possible for M-dwarfs.

A higher metallicity and C/O ratio results in a higher concentration of carbon-bearing species; in particular CH_4 , CO_2 , and CO. Hence, a higher detectability of disequilibrium is expected at these conditions. This is shown in the [Fe/H]-C/O panel, where the region of interest (with dark-blue colors) is associated with super-solar metallicities and super-solar C/O ratios.

In summary, we find that the detectability of disequilibrium could be maximized by focusing on the targets with T_{eff} between 1000 and 1800 K, orbiting around M-

dwarfs, having low surface gravity but high metallicity and a C/O ratio value around unity.

3.5. Classification and Color-diagram

In the first paper in this series (Molaverdikhani et al. 2019), we proposed a new classification scheme for irradiated gaseous planets based on a grid of cloud-free self-consistent models with four classes. Class-I includes planets colder than 600–1100 K. Class-II planets are hotter than Class-I ranging from 600–1000 K to about 1650 K. The boundary between Class-I and II changes with $\log(g)$, metallicity, and stellar type of the host star. Class-III planets have a temperature between 1650 K and 2200 K, and Class-IV planets are hotter than 2200 K. Here we employ the results of our grid of disequilibrium chemistry models to study the effect of vertical mixing on the atmospheric spectra and hence our proposed classification scheme.

As discussed in the first paper, carbon-to-oxygen ratio affects the composition of hot planetary atmospheres in a way that water is expected to be more prominent

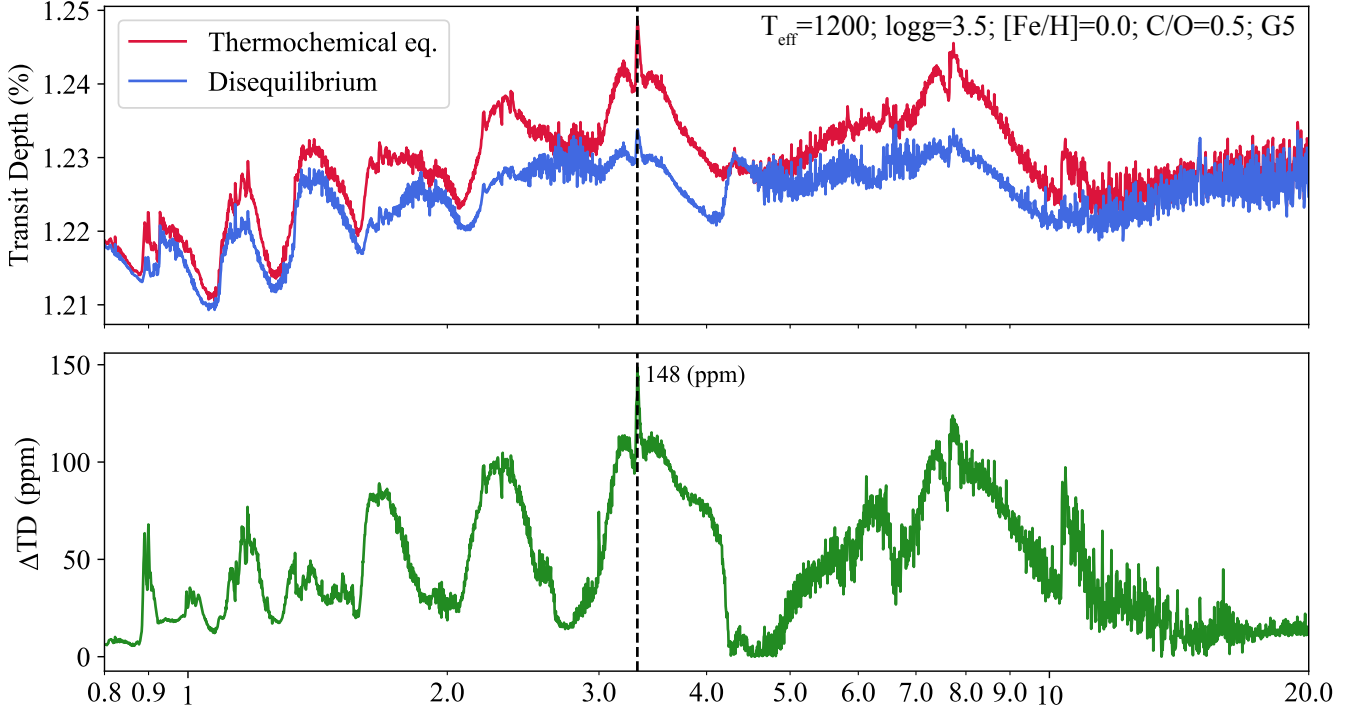


Figure 5. Variation of transmission spectrum due to disequilibrium chemistry for a Jupiter-sized planet orbiting a G5-type star with solar metallicity, $C/O \sim 0.5$, and surface gravity of 3.5. **Top)** Methane abundance decreases as a result of added vertical mixing with $K_{zz} = 10^{12} \text{ cm}^2 \text{ s}^{-1}$ (blue) with respect to the thermochemical equilibrium state (red). **Bottom)** The difference between the two spectra indicates that the CH_4 feature at $3.3 \mu\text{m}$ has the maximum variation within JWST’s wavelength coverage.

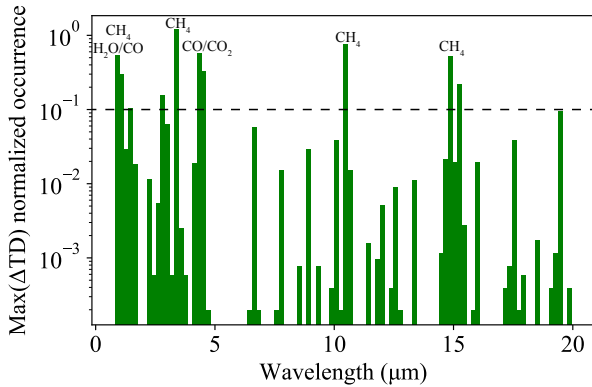


Figure 6. Occurrence rate of maximum variation in the transmission spectra, $\text{max}(\Delta\text{TD})$, within JWST’s wavelength range. Five wavelength regions show the highest occurrences, namely $\sim 1 \mu\text{m}$ (CH_4 , H_2O , or CO), $\sim 3.3 \mu\text{m}$ (mostly CH_4), $\sim 4.5 \mu\text{m}$ (CO_2 or CO), $\sim 12 \mu\text{m}$ (CH_4), and $\sim 15 \mu\text{m}$ (CH_4).

at lower C/O ratios and methane, CO , or HCN to be the dominant chemical products at higher C/O ratios. The spectral decomposition technique provides the necessary tool to find the transition C/O ratio, i.e. the C/O

ratio at which the atmospheric spectra changes from a water- to methane-dominated spectrum. By employing this technique, we estimate the transition C/O ratios for our grid of disequilibrium chemistry models, see Figure 8, for $K_{zz} = 10^{12} \text{ cm}^2 \text{ s}^{-1}$ models.

In general, but not always, vertical mixing on Class-II and III planets cause the transition C/O ratios to decrease for atmospheres with high β . The β factor is a linear combination of surface gravity and metallicity. Higher β values represent deeper photospheres, i.e. at higher pressures. See (Molaverdikhani et al. 2019) for a detailed discussion on the β factor. This is mostly caused by the higher amount of CH_4 at the photospheric level, when β is higher. Its effect is different for atmospheres with low β and vertical mixing increases the transition C/O ratios. These are shown by blue (for low β models) and red (for high β models) vectors on Figure 8 left panel.

The only difference between Class-II and Class-III planets is that in Class-II the atmosphere still contains some oxygen-bearing condensates, but in Class-III planets all those condensates are evaporated. This causes the transition C/O ratios in Class-III to become independent of atmospheric conditions and remain at a con-

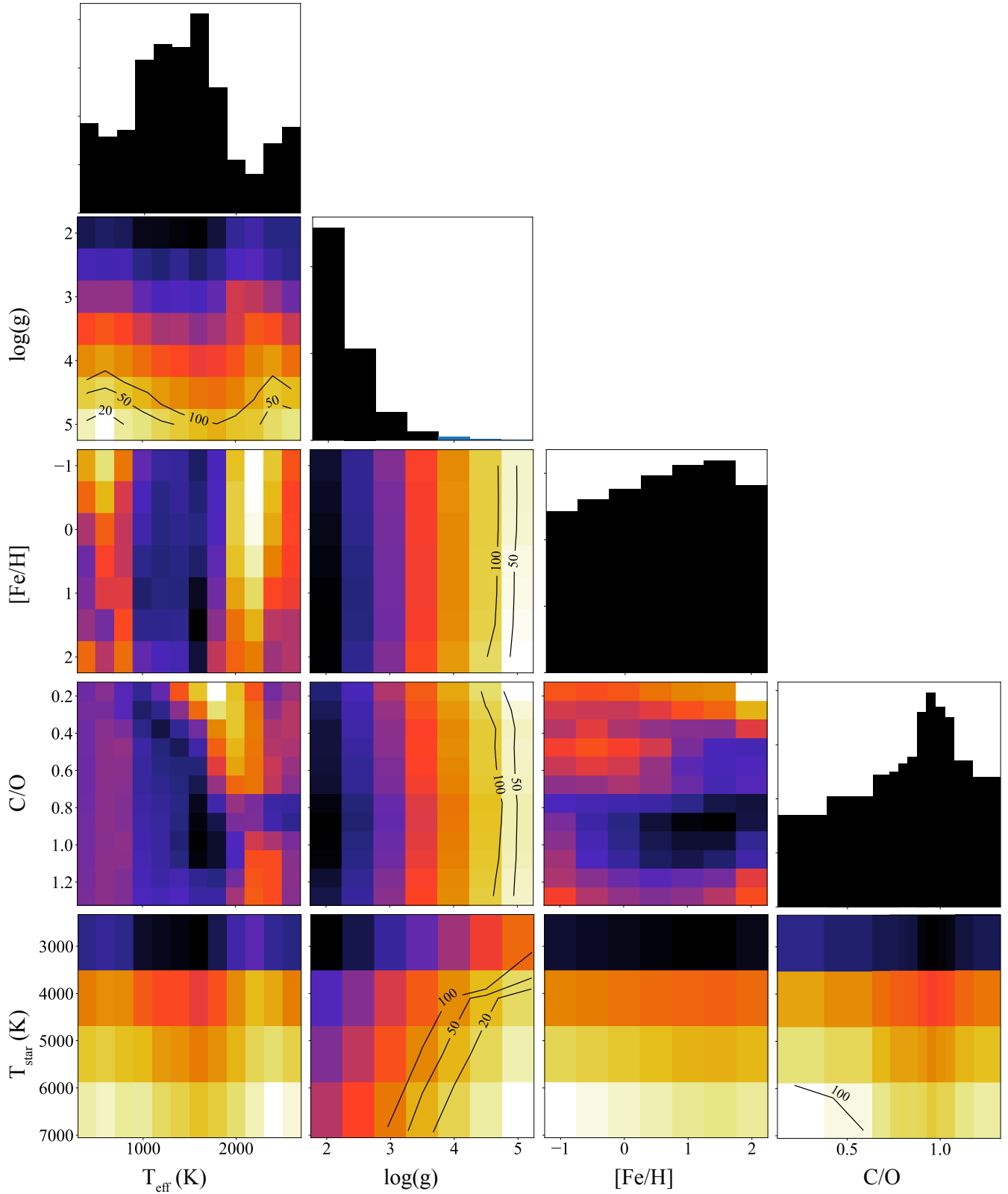


Figure 7. The average maximum variation in the transmission spectra, $\max(\Delta TD)$, due to the disequilibrium for a Jupiter-size planet. Dark-blue represents the parameter-space with the highest $\max(\Delta TD)$. Colormaps are scaled for each panel to show the patterns in more detail. Regions with 20, 50, and 100 ppm levels are shown with counters; 20 and 50 ppm represent the noise levels for NIRISS SOSS and MIRI LRS, respectively (Greene et al. 2016). Panels without the counters have $\max(\Delta TD)$ higher than 100 ppm. The marginal panels (1D black histograms at the top) represent ΔTD of individual atmospheric parameters.

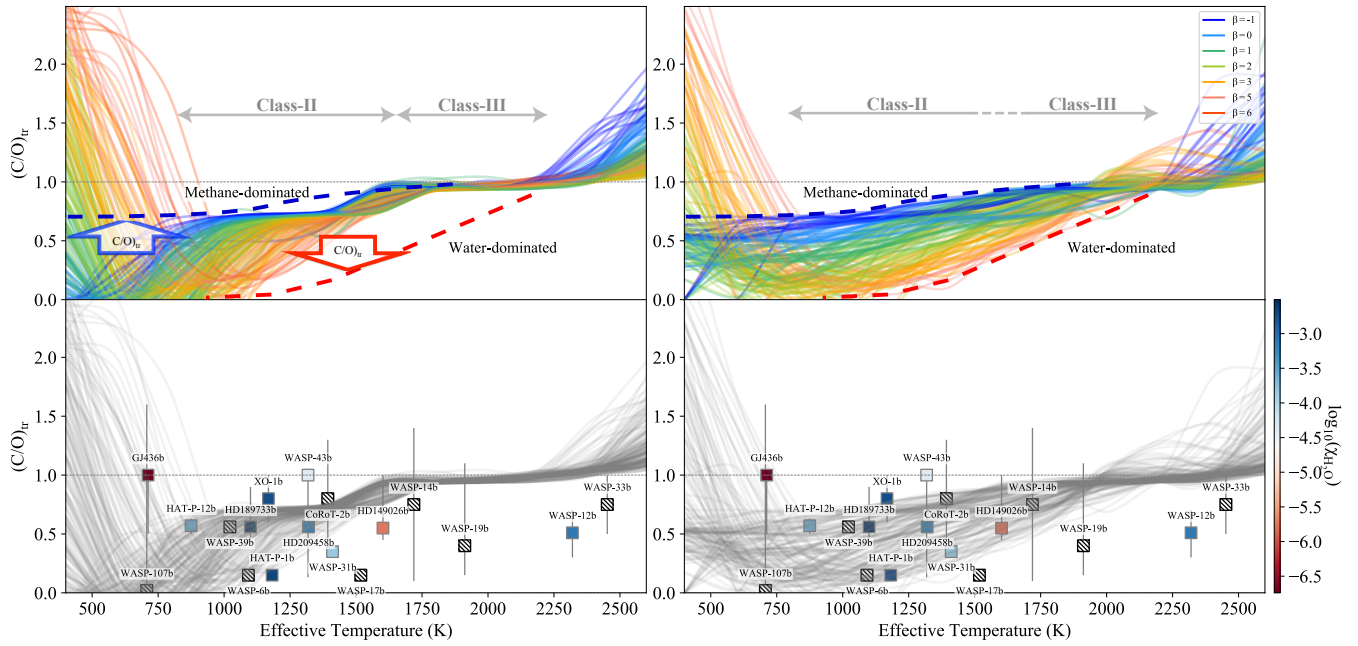


Figure 8. The effect of vertical mixing on the transition C/O ratios. **Upper left)** Transition C/O ratios of thermochemically equilibrium models presented in Molaverdikhani et al. (2019). The transmission spectra above the transition lines are expected to be CH_4 -dominated and below them to be H_2O -dominated. Different colors represent the transition C/O ratio at different β factors. **Bottom left)** The location of exoplanets on the thermochemical equilibrium map with estimated T_{eff} and C/O . **Upper right)** Transition C/O ratios of chemical kinetic models. **Bottom right)** The location of exoplanets with estimated C/O ratio, on the chemical kinetic map. The lines in the bottom panel are gray to increase the visibility of colors for the water content of the observed planets.

stant value of ~ 0.9 . Vertical mixing removes this difference and merges Class-II with III to one extended class; covering the whole range of ~ 900 K to ~ 2000 K in one class.

In Class-I planets, both H_2O and CH_4 are usually the dominant species and have relatively less vertically variant profiles. Hence, their abundance variation at TOA is less sensitive to the vertical mixing. Class-IV planets with $\text{C}/\text{O} < 1.0$ are mostly deficient of CH_4 due to their hot temperatures. Hence their transition C/O ratio remains higher than unity at all time and are usually insensitive to the vertical mixing. However, some Class-IV planets, $T_{\text{eff}} > 2000$ K, with very high β , > 5 , show an increase in their transition C/O ratio due to lower CH_4 abundances at high pressures. Consequently, our proposed four classes of planets based on our grid of cloud-free models can change to a three classification scheme of planets assuming strong vertical mixing in their atmospheres.

Regardless of the naming of these classes, there exists a ‘‘Methane Valley’’ in both thermochemical equilibrium and vertical mixing cases (see Figure 8). The Methane Valley is a region between 800 and 1500 K, where methane is expected to cause the dominant spectral features in the transmission spectra of planets. Hence, a greater chance of CH_4 detection is expected for the planets within this region. The first robust CH_4 detection on an irradiated planet was indeed reported for HD 102195b (Guilluy et al. 2019). This is a Class-II planet with $T_{\text{eq}} \sim 963$ K, within the Methane Valley and consistent with our prediction.

We also calculate the transmission and emission color-maps, using Spitzer IRAC channel 1 and 2, similar to what we presented in the first paper. We note small changes seen in the IRAC emission maps, when going from thermochemical equilibrium to disequilibrium chemistry. Vertical mixing is expected to play a strong role in the atmospheres of cool ($T < 1000$ K), self-luminous atmospheres with low (planet-like) $\log(g)$ (see, e.g., Zahnle & Marley 2014). In such atmospheres the abundances of the cooler upper atmospheric layers is overruled by the abundances mixed up from hot layers at higher pressures, which leads to a significant increase in CO abundance, at the expense of CH_4 . A similar effect appears to occur for a few hundred atmospheres in our grid of +28,000 models, which start to fill in the region with $(F_{3.6} - F_{4.5})/F_{4.5} > -0.5$. This happens for the models with effective temperatures below ~ 900 K and with very small C/O ratios (< 0.25) only (blue points in the low C/O regime in Figure 9). Considering what has been predicted for self-luminous atmospheres, this is unexpected. A likely reason for this

difference is that the atmospheric temperature profiles of irradiated planets are more isothermal than those of self-luminous ones, such that the deeper (higher pressure) regions from which material is mixed up is cooler, and hence richer in CH_4 ².

The color maps do not show any other statistically meaningful differences, see Figure 9, and the two main populations (i.e. CH_4 -driven and CO/CO_2 -driven populations) remain almost invariant. Our results indicate that deviations from the Spitzer equilibrium chemistry color map presented here are most likely due to effects different than the disequilibrium processes studied in our work, with clouds being a strong contender, the effect of which we will study in our upcoming third paper of this series. If disequilibrium should be the culprit for such deviations, it would point to very small C/O ratios (< 0.25).

4. CONCLUSION

In this paper, we introduced our newly developed Chemical Kinetic Model (ChemKM). The code includes a variety of atmospheric processes including photolysis, molecular and eddy diffusion, and condensation and rainout. Other processes, such as atmospheric ablation and escape can also be included. It is also possible to include galactic and solar cosmic rays (GCRs) and scattered UV sources by LIPM in the models.

After verification of individual processes in ChemKM, we compared our results to the Venot (2012) model for HD 189733b. The calculated abundances were consistent between the models except at the μbar regime, where the molecular diffusion and photochemistry are the dominant processes. As a conclusion, we recommend careful consideration of these processes when abundances at TOA have to be calculated.

We used our grid of disequilibrium chemistry atmospheres with six free parameters, planetary effective temperature (T_{eff}), surface gravity ($\log(g)$), metallicity ($[\text{Fe}/\text{H}]$), carbon-to-oxygen ratio (C/O), spectral type of the host star, and vertical mixing ($K_{\text{zz}} = 10^6, 10^9, \text{ and } 10^{12} \text{ cm}^2 \text{ s}^{-1}$), to determine the quenching levels. We propose a new metric, the geometric Coefficient of variation (gCV) of abundances, for a quantitative measure of quenching. We find P_{quench} varies significantly under our self-consistent static TP structure setup. We find that all atmospheric parameters ($[\text{Fe}/\text{H}]$, $\log(g)$, and

² CO to CH_4 conversion is favored at cool, high pressure conditions; see e.g. Lodders & Fegley (2006); Marley et al. (2002); Hubeny (2017); Noll et al. (2000); Skemer et al. (2012); Saumon et al. (2003).

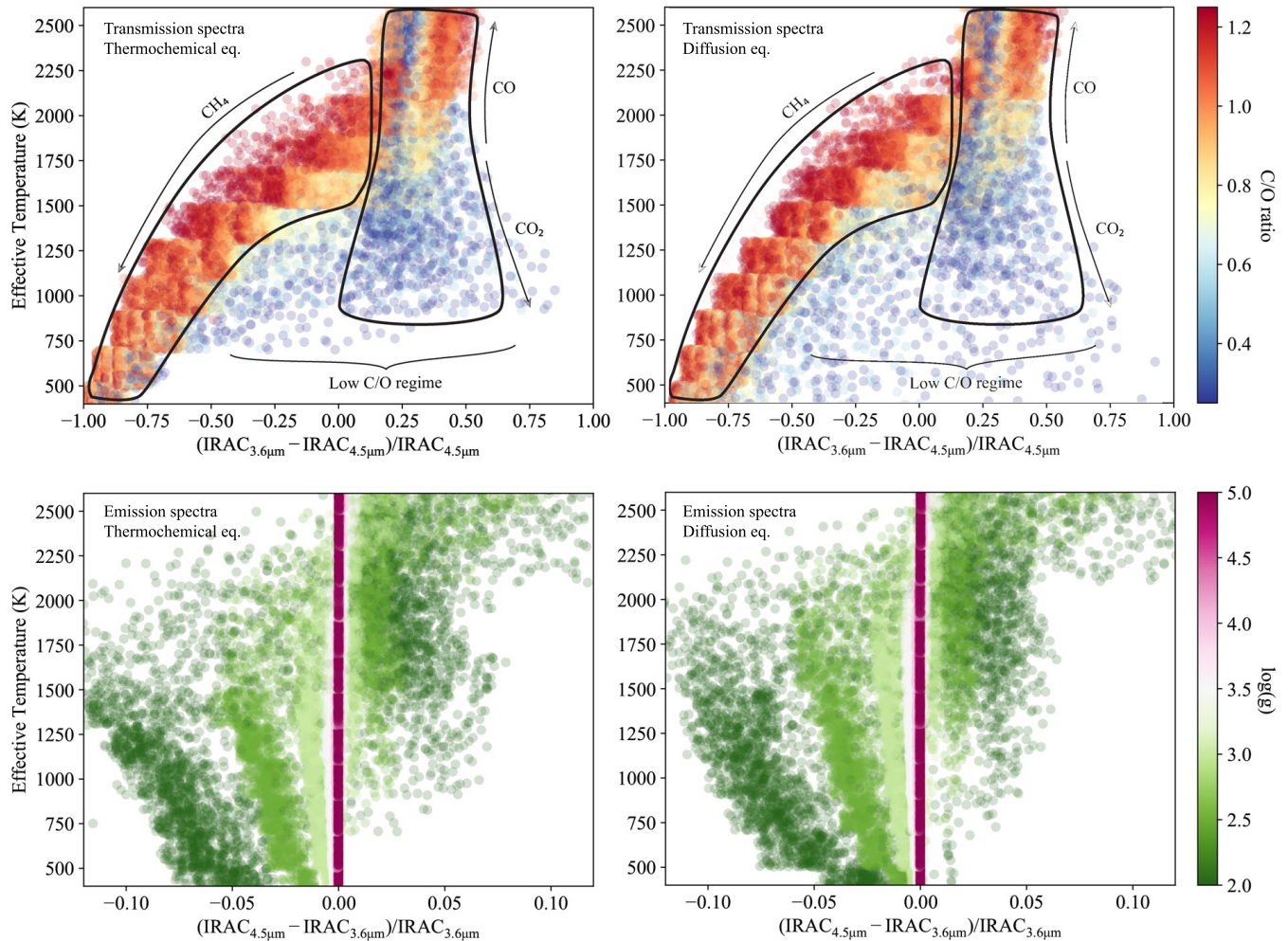


Figure 9. Synthetic Spitzer IRAC color–temperature diagrams for cloud-free atmospheres under thermochemical equilibrium (**left panels**) and diffusion equilibrium (**right panels**) conditions. **Top panels** Color diagram based on emission spectroscopy, i.e., IRAC data describes the secondary eclipse depth at λ (μm). **Bottom panels** Same for the transmission technique, i.e., IRAC data describes the transit depth at λ (μm). No significant difference can be seen between thermochemical and diffusion equilibrium models, except for Class-I planets with very low C/O ratios.

C/O) affect P_{quench} by changing the atmospheric composition.

To explore the detectability of disequilibrium spectral fingerprints due to the molecular and eddy diffusion by JWST, we recommend focusing on the targets with T_{eff} between 1000 and 1800 K, orbiting around M-dwarfs, having low surface gravity but high metallicity and high C/O (see Section 3.4).

We also find that the “Methane Valley” remains largely unchanged by the inclusion of vertical mixing. This is a region between 800 and 1500 K, where a greater chance of CH_4 detection is expected. Indeed, the first robust CH_4 detection on an irradiated planet was within this region (Guilluy et al. 2019); supporting our prediction from Molaverdikhani et al. (2019). We argued in

Paper-I that the detection of CH_4 or the lack of such detection, could hint at the prevalence of cloud formation or disequilibrium chemistry. Here we find that disequilibrium unlikely to change this picture significantly. Thus, characterization of planetary atmospheres within this parameter space is expected to provide a diagnostic tool to identify cloud formation condition.

Our further analysis showed that the two main populations in the Spitzer IRAC’s emission color-maps remain largely unchanged, when including mixing. Although we note some differences between the two maps for the models with effective temperatures below ~ 900 K and with very small C/O ratios (< 0.25), see Figure 9. Therefore any deviation of observational points from these color-maps is likely to be due to the

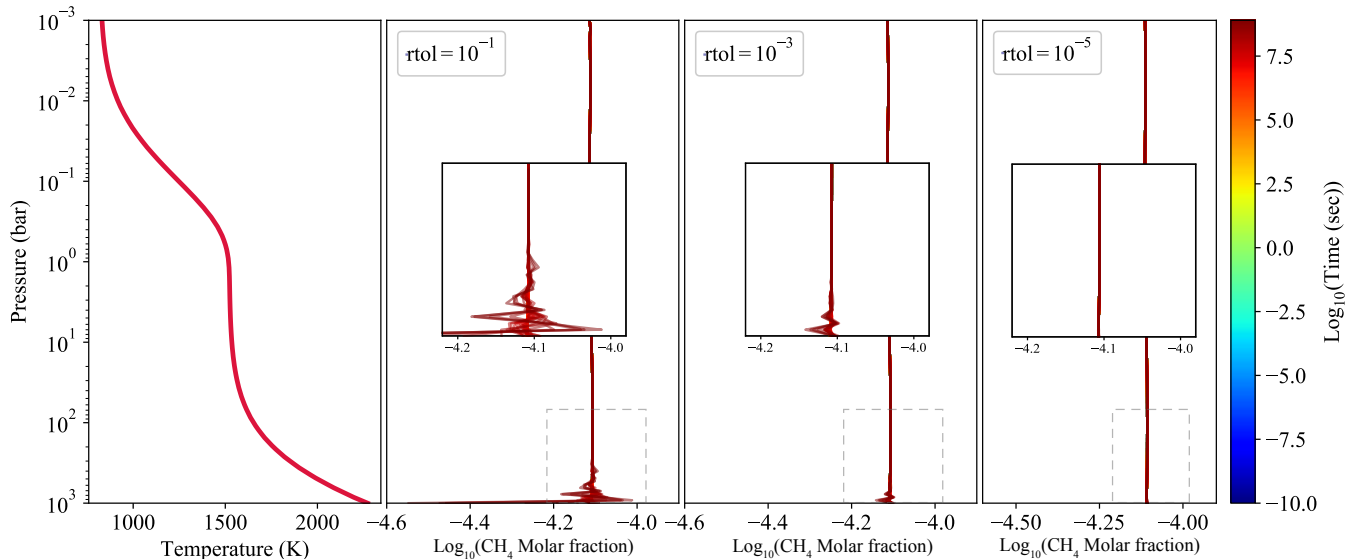


Figure 10. Numerical instability due to the choice of relative tolerance, $rtol$, in the numerical solver. Poor numerical convergence occurs at high temperature-pressure regions of the atmosphere, unless a proper $rtol$ value is chosen. **Left)** Temperature profile of a typical Hot Jupiter with $T_{\text{eff}}=1500$ K. **Rest of panels)** show the time evolution of CH_4 vertical abundance. Initial abundances are calculated by Gibbs free minimization and are expected to remain the same throughout the simulation. Three simulations are the same, except their choice of $rtol$. Simulations with $rtol=10^{-1}$ and 10^{-3} show non-negligible numerical instabilities, whereas $rtol=10^{-5}$ results in an adequately accurate abundance estimation.

presence of clouds and not disequilibrium chemistry, but the effect of mixing for cold planets with very low C/O ratios could be significant.

Clouds can potentially change the TP structure, composition, and ultimately the spectra of planetary atmospheres. In the next paper in this series, “From cold to hot irradiated gaseous exoplanets”, we investigate how cloud formation affect the atmospheric spectra and what types of planets are most affected by this process.

5. ACKNOWLEDGMENT

The authors would like to thank Dr. Dmitry A. Semenov for constructive feedbacks during the development of ChemKM and would like to thank Dr. Olivia Venot, Dr. Juliane Moses, Dr. Eric Hébrard, and Dr. Shang-Min Tsai for providing their chemical networks.

We used the online database KIDA for some kinetic data. This research has made use of the NASA Exoplanet Archive, which is operated by the California Institute of Technology, under contract with the National Aeronautics and Space Administration under the Exoplanet Exploration Program. The authors would like to thank the anonymous reviewer for her/his helpful and constructive comments that greatly contributed to improving the final version of the paper.

6. SOFTWARES

Employed softwares and packages in this work are as follow:

Software: petitCODE (Mollière et al. 2015, 2017), ODEPACK (Hindmarsh 1983), and ChemKM (this work).

APPENDIX

A. METHODOLOGY

A.1. Chemical solvers

The challenge of most chemical kinetic models is to find an efficient method to solve the system of ODEs, which are stiff and sparse in nature. Diversity of physical and computational complexities in the simulation of planetary atmospheres results in different degrees of stiffness, and hence complicates the choice of a fast and yet accurate sparse-stiff ODE solver. We have examined two well-established ODE solver packages from the ODEPACK collection, namely DLSODE (Double precision Livermore Solver for Ordinary Differential Equations) and DVODPK (Double precision

Variable-coefficient method for Ordinary Differential equations using Preconditioned Krylov method) (Hindmarsh 1983).

The DLSODE solver is based on the older GEAR and GEARB packages, and has the same numerical core. In GEAR, the error is controlled only by one scalar relative error tolerance, called EPS. In DLSODE, on the other hand, the user can set both relative and absolute error tolerances, rtol and atol, which optionally can be scalar or vector. The choice of these error tolerances are usually a compromise between the accuracy and speed of the simulation, i.e. a smaller error tolerance makes the solutions more accurate, but at the same time it increases the computational time, because the solver requires more iterations to achieve the specified tolerance. Our extensive examination of rtol and atol indicates that the computational time scales with rtol exponentially, but the choice of atol has no significant effect on the computational time. Therefore, we choose a very small atol, 10^{-99} , as the default atol value for our simulations.

A choice of rtol= 10^{-1} , 10^{-2} or 10^{-3} can be used for a rapid verification of the system’s behavior, but we recommend rtol= 10^{-5} to insure numerical stability when the production and loss terms are large, but of the same order, i.e. the system is at or close to \sim steady state, see Figure 10. In this figure we present a worst case scenario where the atmosphere is initialized at its equilibrium state and is forced to remain at that condition by using chemical kinetic calculations. This is not the usual setup and planetary models normally include at least one disequilibrium process such as diffusion. The numerical instability at rtol= 10^{-1} and 10^{-3} are shown in Figure 10 are for CH_4 abundance profiles but almost all other species behave similarly. Diffusion usually relaxes the limit on rtol for achieving the numerical stability and introduces a damping effect. In addition, stronger diffusion forces the system to reach the steady state faster; leading to less propagated numerical errors in the steady state solution of the system. Hence, a lower rtol can be selected when stronger diffusion mechanism are in play.

It is also possible to specify the tolerances as vectors; i.e. assigning each species its own relative and absolute tolerances. This treatment could be used, for instance, on a reactant that is completely depleted in at least one vertical layer. In this paper, we use scalar values for rtol and atol with the values of 10^{-5} and 10^{-99} , respectively.

DVODPK employs iterative methods to solve linear algebraic systems. It is based on orthogonal projection techniques, which approximate a solution of the linear system from a Krylov subspace. This technique is more advanced and more efficient in comparison with DLSODE’s method (Nejad 2005), however, its usage requires decomposition and initialization of the Jacobian matrix. This is not a trivial task and our investigations revealed that this technique requires adaptation of the Jacobian decomposition for every new simulation. Moreover, DVODPK’s performance changes significantly with the physical conditions considered in the model, such as inclusion of condensation, ablation, outgassing, etc.

On top of all is DVODPK’s inefficiency under planetary atmosphere conditions. Figure 11 illustrates the DVODPK’s running time for a suite of 0D simulations over a broad range of densities and temperatures. We found DVODPK is less efficient to solve ODEs at higher density and temperature conditions, and hence is not suitable for the application to planetary atmosphere kinetic simulations. Therefore we use DLSODE from the ODEPACK library as our default solver.

A.2. Chemical networks

Answering the question of which set of reactions, i.e. chemical network, must be used in a chemical kinetic model is arguably the most important question that should be addressed before setting up a model. One could establish a chemical network from the scratch by doing a standard literature search for the thermodynamic polynomial coefficients, reaction rate constants, UV cross sections, and branching ratios, or alternatively employ the commonly used networks in the field. Here we took the latter approach as the establishment of a new network is beyond the scope of this study. Currently, nine chemical networks are available in ChemKM: Moses’s Hot Jupiter network (Moses et al. 2011), Venot’s 2012 network (Venot et al. 2012), Hebrard’s Titan network (Hébrard et al. 2012), Hebrard’s C_3H_p network (Hébrard et al. 2013), Venot’s full network (Venot et al. 2015), Vulcan H-C-O network (Tsai et al. 2017), Moses’s ice-giants network (Moses et al. 2018), Venot’s reduced network (Venot et al. 2019), and Pearce’s HCN network (Pearce et al. 2019), which differ in the complexity, size (number of species and reactions), type of chemistry (reversible/irreversible, H-C-O species, H-C-O-N species, HCN network), and the temperature range over which the chemical schemes are valid, see Table 1.

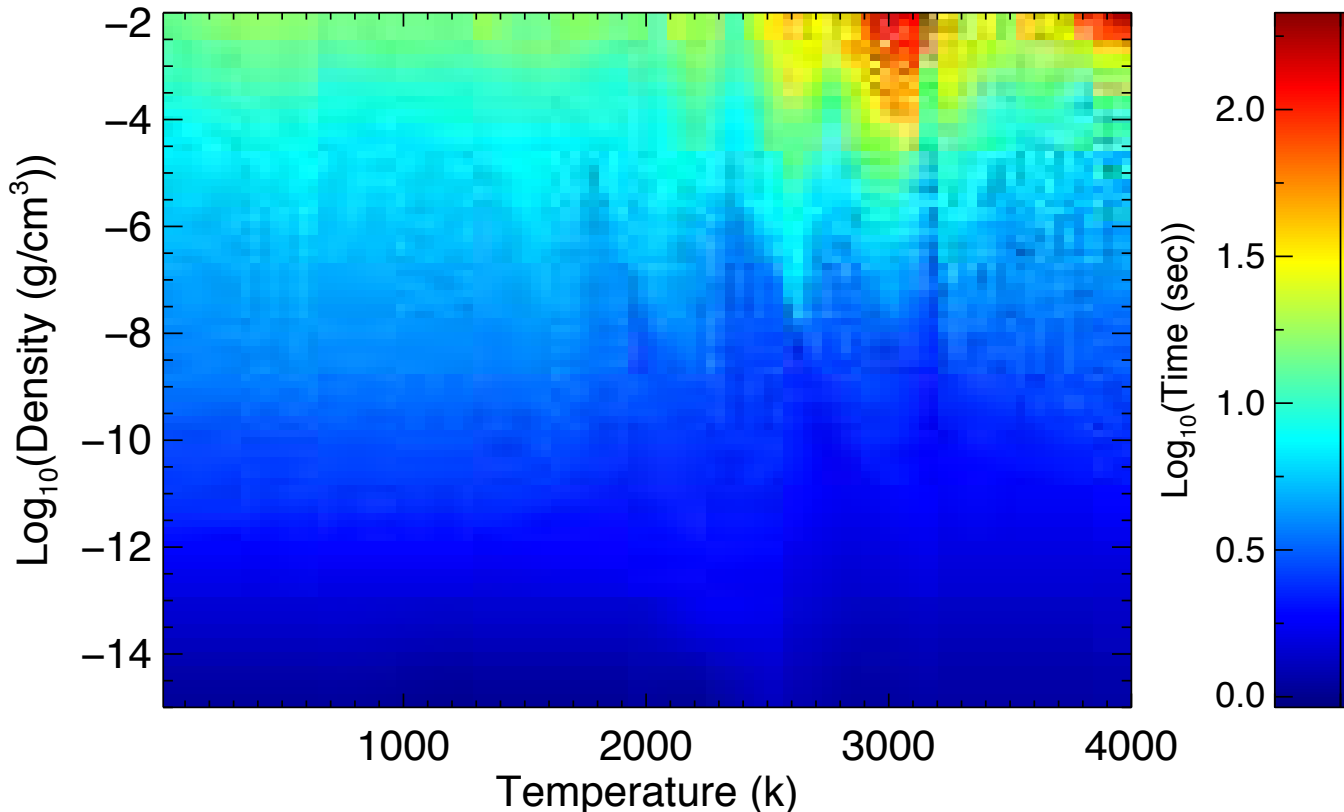


Figure 11. DVODPK’s running time for a suite of 0D simulations over a broad range of densities and temperatures. The solution of the system of ODEs by DVODPK appears to be less efficient at higher density and temperature conditions.

| Chemical Network | Elements | Species | Reactions | Reference |
|--------------------|----------|---------|-----------|---------------------|
| Moses Hot Jupiters | H-C-O-N | 90 | 800 | Moses et al. 2011 |
| Venot 2012 | H-C-O-N | 103 | 963 | Venot et al. 2012 |
| Hébrard 2012 | H-C-O-N | 135 | 788 | Hébrard et al. 2012 |
| Hébrard 2013 | H-C-O-N | 90 | 941 | Hébrard et al. 2013 |
| Venot 2015 | H-C-O-N | 238 | 2011 | Venot et al. 2015 |
| VULCAN H-C-O | H-C-O | 29 | 300 | Tsai et al. 2017 |
| Moses Ice-giants | H-C-O | 69 | 385 | Moses et al. 2018 |
| Venot reduced | H-C-O-N | 29 | 181 | Venot et al. 2019 |
| Pearce HCN | H-C-N | 11 | 42 | Pearce et al. 2019 |

Table 1. General characteristics of chemical networks implemented in **ChemKM**. He and Ar are excluded from the list of species. The reverse reactions calculated by using the thermodynamic principle of microscopic reversibility are not included.

ChemKM is able to handle a variety of reaction types including KIDA’s standard formulations³ (e.g. Modified Arrhenius reactions, third body assisted reactions with Troe (Troe 1983; Gilbert et al. 1983), and SRI (Stewart et al. 1989; Kee et al. 1989) falloff functions) as well as Vuitton (Vuitton et al. 2011) and Jasper (Jasper et al. 2007) formulations. Therefore **ChemKM** can easily accept new networks as the input of models.

³ <http://kida.obs.u-bordeaux1.fr>

A.3. Condensation and rainout

Observations of planets suggest the presence of clouds nearly in all classes of planets with substantial atmosphere. For instance, Venus is fully covered by a thick cloud layer, containing mostly H_2SO_4 particles (e.g., [Molaverdikhani et al. 2012](#)). On Earth, water clouds produce a patchy scenery, covering about 70% of the surface with optical depth of larger than 0.1 (e.g., [Stubenrauch et al. 2013](#)). Despite its tenuous atmosphere, conditions on Mars allow for the formation of what is mostly believed to be high-altitude CO_2 clouds (e.g., [Clancy & Sandor 1998](#)).

Outer planets in the solar system have even colder atmospheres, resulting in more efficient cloud-forming environments. Observations and simulations support the formation of NH_3 , NH_4SH , and H_2O Jovian clouds above 10 bar. Their altitude and thickness, however, could vary both spatially and temporally ([Pater et al. 2016](#)). Clouds with similar compositions are expected to form on Saturn; owing to their similarities in temperature structure and bulk composition. However, there are some subtle differences that result in vertically more extended clouds and higher amount of gas above the cloud-bases on Saturn ([West et al. 2009](#); [Atreya et al. 1999](#)). Saturn and Neptune observations also show evidence of CH_4 and H_2S clouds in addition to NH_3 , NH_4SH , and H_2O clouds, due to their colder environments ([Irwin et al. 2018, 2019](#)).

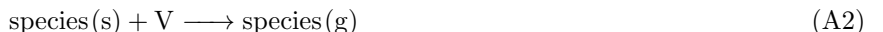
Although not a planet anymore, Pluto, as seen by the New Horizon spacecraft, is covered by layers of hazes ([Gladstone et al. 2016](#); [West 2017](#)), likely due to condensation of hydrocarbons and nitriles such as C_2H_2 , C_2H_4 , C_2H_6 , and HCN ([Gao et al. 2017](#)). We also have to mention Titan, since it has a unique and substantial atmosphere, with hydrocarbon and nitrile cloud types. This includes HCN , HC_3N , CH_4 , C_2H_2 , and C_2H_6 coated particles ([Lavvas et al. 2011](#)).

Clouds on gaseous planets beyond the solar system have also been observed. [Sing et al. \(2016\)](#) studied the transmission spectra of 10 Hot Jupiters and concluded that there is very likely a continuum of exoplanetary atmospheres; covered by haze and clouds with a variety of compositions. For instance, a nearly flat transmission spectrum of GJ 1214b (a sub-Neptune planet with an equilibrium temperature of 580 K) is consistent with a planet which is fully covered by clouds; most likely composed of ZnS and KCl ([Kreidberg et al. 2014](#)). Hotter Class-II gaseous exoplanets⁴ with a temperature range of ~ 1000 K to ~ 1650 K could have Na_2S , MnS , Fe , Al -oxides, or silicate clouds such as Mg_2SiO_3 and Mg_2SiO_4 clouds. Even Ultra-Hot Jupiters ($T \gtrsim 2500$ K) are expected to have cloud formation on their nightside ([Helling et al. 2019](#); [Keating & Cowan 2018](#)), which could be dragged toward the dusk terminator of the planet and potentially contribute in the transmission spectra and transit depth of these planets (e.g. Helling in perp.). For a recent review on exoplanet cloud formation see [Helling \(2019\)](#).

All these studies suggest the importance of condensation and particle formation in planetary atmosphere models. However, including even a simplified microphysics model, such as atmospheric models by [Rossow \(1978\)](#), in a chemical kinetic model demands high computational resources mostly because of the shorter timescales that condensation and evaporation operate on relative to the vapor transport or gas-phase chemistry timescales ([Moses 2014](#)). Hence a simpler approach is usually taken.

[Dobrijevic et al. \(2010\)](#) assumed condensation of species when their abundances reach their saturation level. After hitting this condition, they did not solve the continuity equation of that species at the given altitude; resulting in numerical stability and high computational efficiency of the scheme. A consequence of this approach is that the abundance of the condensed species follows its saturation curve perfectly. But condensation processes could occur at different saturation levels. Capillary condensation is an example, which through this mechanism the vapor condensation occurs below the saturation vapor pressure ([Stokes & Evans 1997](#)).

[Moses et al. \(2000a,b\)](#) treated the condensed phase of a species as a separate species that is produced by condensation and lost by evaporation through the following reactions:



where “dust” represents the condensation nuclei (CN) and must be provided, “V” represents a dummy molecule and its number density assumed to be 1 cm^{-3} at all atmospheric levels, and the subscripts (g) and (s) refer to the gas and condensed phases, respectively. This scheme assumes the pre-existence of CN in the atmosphere; allowing

⁴ See the first paper in this series for the classification scheme ([Molaverdikhani et al. 2019](#)).

the condensation of materials on these sites. They estimated the rate of these reactions by assuming steady-state diffusion-limited condensation and followed Seinfeld (1986) rate estimations.

We follow a similar approach to account for the condensation, but with slightly different rate estimations adapted from Seinfeld & Pandis (2012) as follow:

$$J_c = 4\pi R_p D_g (c_\infty - c_s) \quad (\text{A3})$$

where J_c is the total flow of the species toward the particle (moles sec^{-1}), R_p is the particle’s radius, D_g is the diffusivity of the species in the atmosphere, c_∞ is the concentration of the species far from the particle, and c_s is its vapor-phase concentration at the particle surface. It is evident that when $c_\infty > c_s$ then the species flows toward the particle and if $c_\infty < c_s$ it moves away from it. c_s can be estimated from the vapour pressure of species at any given temperature (vapour pressure data of more than 1700 substances are provided in Haynes (2016) and being updated regularly). To consider the condensation in ChemKM, the user is only required to provide a list of desired species to condense. The code then internally handles the addition of “dummy” reactions and condensed phase of species.

Gravitational acceleration leads to the settlement of condensed particles, i.e. rainout, which tends to remove the condensed materials from the atmosphere. Hence, not including the rainout could cause some discrepancies between the observations and models. Two well-known cases are the detection of H_2S gas on Jupiter (Niemann et al. 1998) and the presence of gaseous alkalis in cool brown dwarf and exoplanet atmospheres (Marley et al. 2002; Morley et al. 2012; Line et al. 2017; Zalesky et al. 2019). On Jupiter, Fe could deplete all sulphur content from the upper atmosphere through condensation of FeS; leaving no sulphur to form H_2S . Adding a Fe-rainout mechanism, however, could deplete all Fe from those regions, hence allowing H_2S to form. Similarly, on brown dwarfs and exoplanets, retaining the silicates at high altitudes can eventually lead to the formation of alkali feldspars; resulting in the depletion of alkalis from the upper atmosphere. Including silicate-rainout processes could prevent such an outcome by removing the silicates from those regions (e.g., Mollière et al. 2015). As an option in ChemKM, this effect can be included by removing the condensates as soon as they condense. A more sophisticated rainout scheme is under development to take into account a proper estimation of the drag force upon the particles and approximation of the settling velocity.

A.4. Ablation and escape

Ablation of micro-meteoroids during atmospheric entry is thought to be a potential source of volatile gases (such as H_2O , CO, CO_2 , and SO_2) that cannot be maintained at the upper atmosphere of planets otherwise. These species could change the chemistry and dynamics of the upper layers. For instance, photolysis of the ablated water produces hydroxyl radicals (OH) (Moses & Poppe 2017), which can react with many other species and cause new reaction pathways and products. Although the details of such processes (even on Earth) is not fully understood (e.g., Hawkes et al. 2008), usually an ablation rate for each species can be estimated based on the observations of the upper atmosphere of planets through a retrieval procedure (Moses 1992; Hörst et al. 2008; Moses & Poppe 2017).

Atmospheric escape is another process in action at the outermost layers of planetary atmospheres. Several atmospheric escape mechanisms have been identified so far; most of which are non-thermal processes, such as pickup by stellar-wind, bulk escape through magnetic flux ropes, or sputtering (e.g., Hunten 1982). While these processes could be the dominant escape mechanisms on colder planets (e.g., Brain et al. 2015; Jakosky et al. 2015), hydrodynamic escape (as one of the thermal processes) is believed to be, at least, as important as non-thermal mechanisms for hot exoplanets (e.g., Salz et al. 2016). Including all these processes into a chemical kinetic model would be a major task and computationally expensive. Thus, a simplified approach (e.g., Moses et al. 2018; Dobrijevic et al. 2014; Hébrard et al. 2013) could be useful. In this approximation, an escape rate is provided for each species at the top of the atmosphere (TOA) and species are removed from the uppermost layer by this rate.

Although gaseous planets have no solid surface, a virtual boundary can be defined as well. For the adequately hot planets, the bottom layer can be selected at a high pressure, where the atmosphere remains at thermochemical equilibrium. However, for cold gaseous planets, their upper troposphere, where a cold-trap is formed, is usually selected to set a boundary layer condition for the chemical models as the bottom layer in the kinetic models is usually not at the thermochemical equilibrium and the local atmosphere is likely prone to the disequilibrium processes. This setting provides more flexibility at the bottom layer of chemical models. For instance, it can be used to estimate the vertical CH_4 vapor flux that makes it past the tropopause cold trap of Uranus and Neptune (e.g., Moses et al. 2018).

These processes can be included by setting the flux rate of species at the top of the atmosphere. Similarly, outgassing and deposition can be included by setting the flux rate of species at the bottom boundary layer in ChemKM.

A.5. Cosmic rays and scattered Ly-alpha by LIPM

Galactic and solar cosmic rays (GCRs) are the main source of ionization at altitudes below 55–60 km on Earth (Velinov 1968; Bazilevskaya 2000); shaping Earth’s stratosphere and thermosphere. GCRs are also the main driving factor of Titan’s photochemistry at pressures between 1 and 50 mbar. Particularly GCR-cascade dissociates N_2 , a crucial process to synthesis nitrogen organics such as HCN (e.g., Capone et al. 1983). GCRs have shown to be important on Neptune’s (e.g., Selesnick & Stone 1991; Lellouch et al. 1994; Aplin & Harrison 2016), Titan’s (e.g., Molina-Cuberos et al. 1999; Yung et al. 1984), and likely exoplanets’ (e.g., Helling et al. 2011; Rimmer & Helling 2013; Scheucher et al. 2018) upper atmospheres, too. A list of GCR reactions along with their rate profiles can be provided to the current version of ChemKM for the inclusion of GCRs. A new GCR module is under development to self-consistently calculate the GCR rates.

Isotropic source of stellar background UV radiation and solar Lyman- α photons that are scattered from atomic hydrogen in the local interplanetary medium (LIPM) are important dissociation/ionization sources at weakly irradiated environments (e.g., Strobel et al. 1991; Moses 1991; Bishop et al. 1998), such as polar regions and nightside of closely orbiting planets or the entire atmosphere of planets orbiting at large distances from their host stars. A wavelength dependent flux of these irradiation sources can be provided to ChemKM to be included in the model.

A.6. Initialization

Once all desired physics in the model are set up, one should provide the initial conditions for the temperature-pressure (TP) and abundance profiles. The current version of ChemKM only considers the TP structure statically; i.e. the TP structure does not change as abundances evolve with time. Abundances can be initialized with two options: 1) by providing the elemental abundances or 2) by providing the molar fraction of any desired species at $t_0=0$.

As a first step, it is possible to calculate the thermochemical equilibrium abundances of species through Gibbs free minimization. We use a slightly modified version of petitCODE’s easy_chem module to perform this (Mollière et al. 2017). Alternatively, the thermochemical equilibrium can be achieved through kinetic calculations. The first approach is usually more suitable, unless the temporal evolution of a system to its thermochemical equilibrium state is as of interest.

Finally, depending on what physical processes are considered in the model, other inputs are also required; for instance the vertical mixing coefficient profile for the eddy diffusion or the influx rates.

B. MODEL VERIFICATION

B.1. Numerical integrator

We start the verification of the code by showing how the DLSODE numerical integrator performs. Figure 12 shows the numerical and analytical solutions of the following system of ODEs:

$$\begin{aligned} \frac{dy_1}{dt} &= -y_2 \\ \frac{dy_2}{dt} &= y_1 \end{aligned} \tag{B4}$$

where y_i is the abundance of species i at any given time, t . Abundance variation of each species depends on one another, hence the system is coupled. The analytical solution of this simple system is as follow, assuming $y_1(0) = y_2(0) = 1.0$:

$$\begin{aligned} y_1 &= \text{Cos}(t) - \text{Sin}(t) \\ y_2 &= \text{Cos}(t) + \text{Sin}(t) \end{aligned} \tag{B5}$$

The results of analytical and numerical solutions are in agreement, hence the numerical performance is assured within the numerical errors.

B.2. Thermochemical equilibrium

Because of the relatively high temperatures at the photosphere of most of known giant exoplanets, simulations of their atmospheric chemistry usually require the consideration of reversible reactions in the model. One issue that have

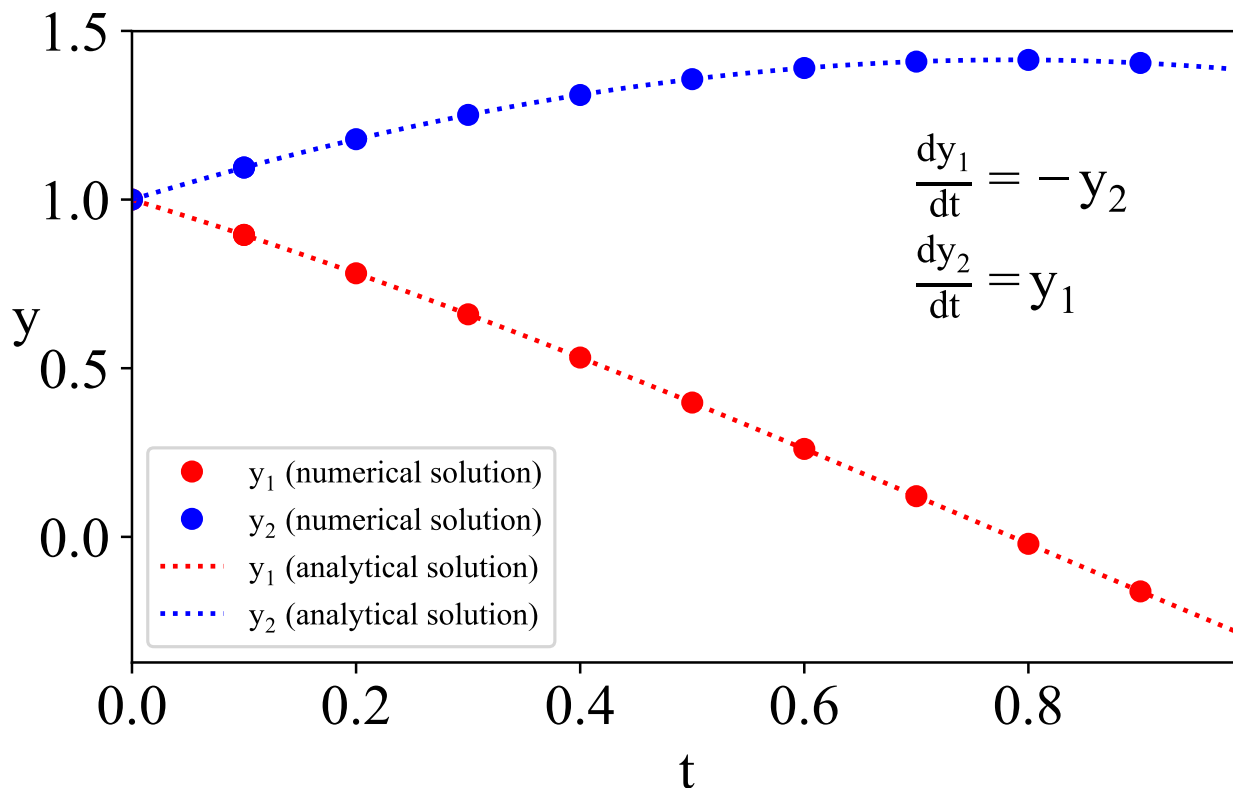


Figure 12. Numerical integrator’s performance for a simple case. The results are compared with the analytical solution of the system. They agree within the numerical errors.

been addressed by previous studies as well (e.g. Moses et al. (2011); Venot et al. (2012); Drummond et al. (2016)) is the unavailability of rate coefficients for most reverse reactions. A common workaround is to calculate these rates as the ratio between the forward rate constant and the equilibrium constant. The equilibrium constant, therefore, can be calculated by using NASA thermodynamic polynomial coefficients (McBride et al. 2002). Inclusion or exclusion of reverse reactions in ChemKM is optional, but if it is chosen to be included then it follows the above described method to calculate the reverse rate coefficients.

Taking this approach ensures the consistency of kinetics and thermodynamics steady state solutions. Figure 13 shows this consistency and compares the results of a simple 0D model at $T=1560$ K and $P=10$ bar for a kinetic chemical model with reversible reactions (curves) and thermodynamic equilibrium calculations (straight thin dotted lines). The kinetic model reaches the thermodynamic equilibrium after 10^7 sec with molar fractions practically being identical. Initial atomic abundances (red lines) deplete as molecules (blue lines) are being produced. Obviously, the chemical evolution of reactants depends on the choice of chemical network. For this test, and all other verification tests in this section, we employ the Venot et al. (2012) kinetic network as a verified and benchmarked chemical network.

Figure 14 provides a similar comparison for a 1D model. Neither our 0D nor the 1D model includes mixing or photolyses for these two tests. The temporal evolution of abundances are color-coded by time where green to red shows the progress in time from 10^{-10} sec to 1.6×10^{18} sec (beyond the age of universe). We show a chemically important atom, $N(^4S)$, one oxygen-bearing major opacity molecule, H_2O , and one expectedly abundant carbon-bearing molecule at high temperatures, HCN, as examples. It is evident that the abundances at kinetically steady state (dark red) are in agreement with their thermodynamic equilibrium values (gray lines) when the local temperature is adequately high (usually above 1000 K). The $N(^4S)$ and HCN abundances at pressures between 10^{-2} and 10^{-8} bar have not fully

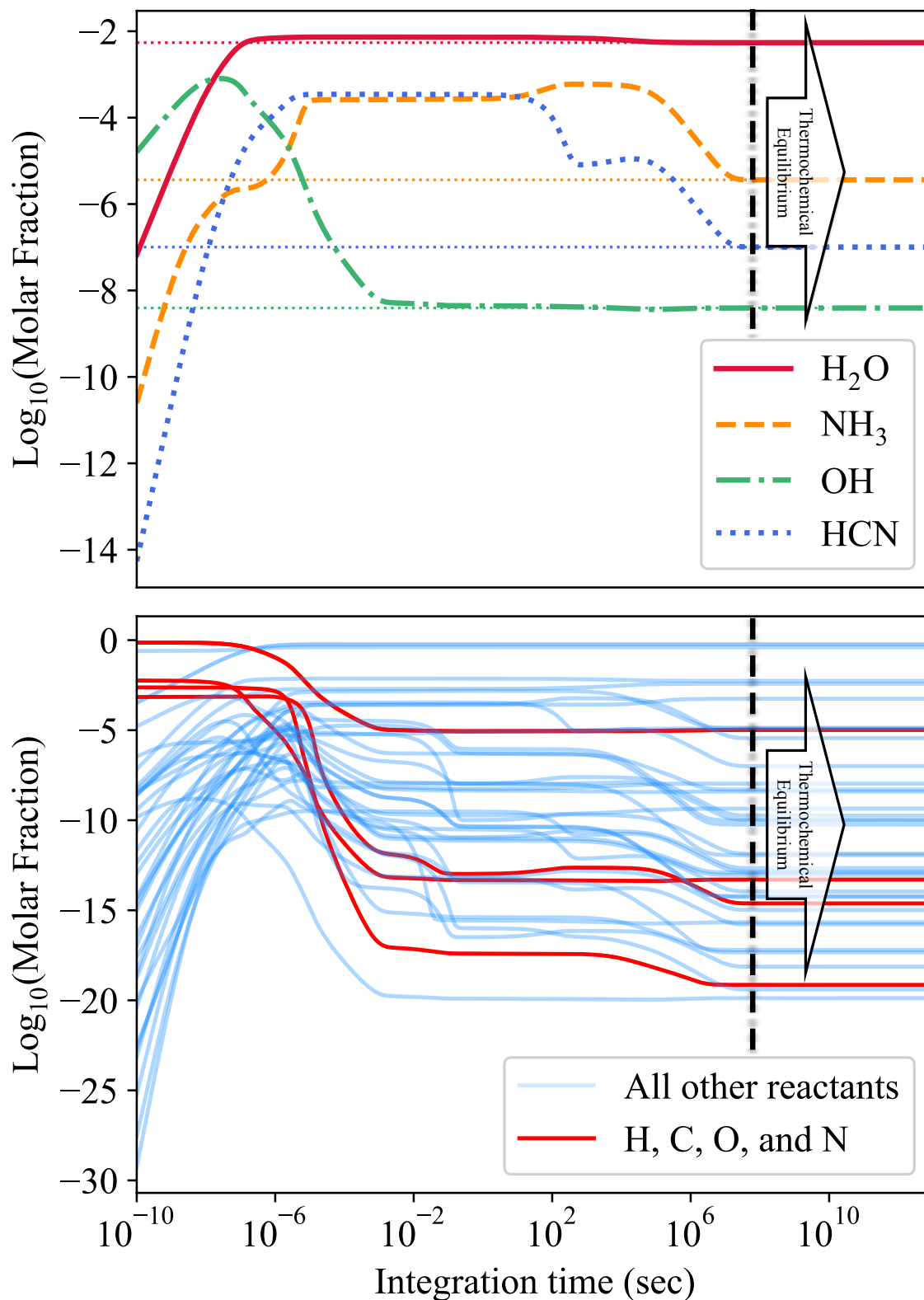


Figure 13. Consistency of the thermodynamic equilibrium composition (dotted straight lines) and ChemKM's kinetic steady state solutions in a reversible system of reactants in a 0D model setup with $T=1560$ K and $P=10$ bar. The result of the thermochemically reversed model is shown as a function of integration time for different species. **Top)** Evolution of H_2O (solid red), NH_3 (dashed orange), OH (dashed-dotted green), and HCN (dotted blue), until they reach their thermochemical equilibrium abundances. **Bottom)** Evolution of H_2 , He , H , CO , H_2O , CH_4 , N_2 , NH_3 , CO_2 , HCN , C_2H_2 , O_2 , $\text{O}(^3\text{P})$, $\text{O}(^1\text{D})$, C , $\text{N}(^4\text{S})$, $\text{N}(^2\text{D})$, OH , CH_3 , $^3\text{CH}_2$, $^1\text{CH}_2$, CH , NH_2 , NH , H_2CO , HCO , CN , C_2H , NO , HNO , NCO , HNCN , HCNO , C_2H_3 , C_2H_4 , C_2H_5 , and C_2H_6 abundances. Atomic abundances (red lines) deplete as molecules (blue lines) are being produced under this condition.

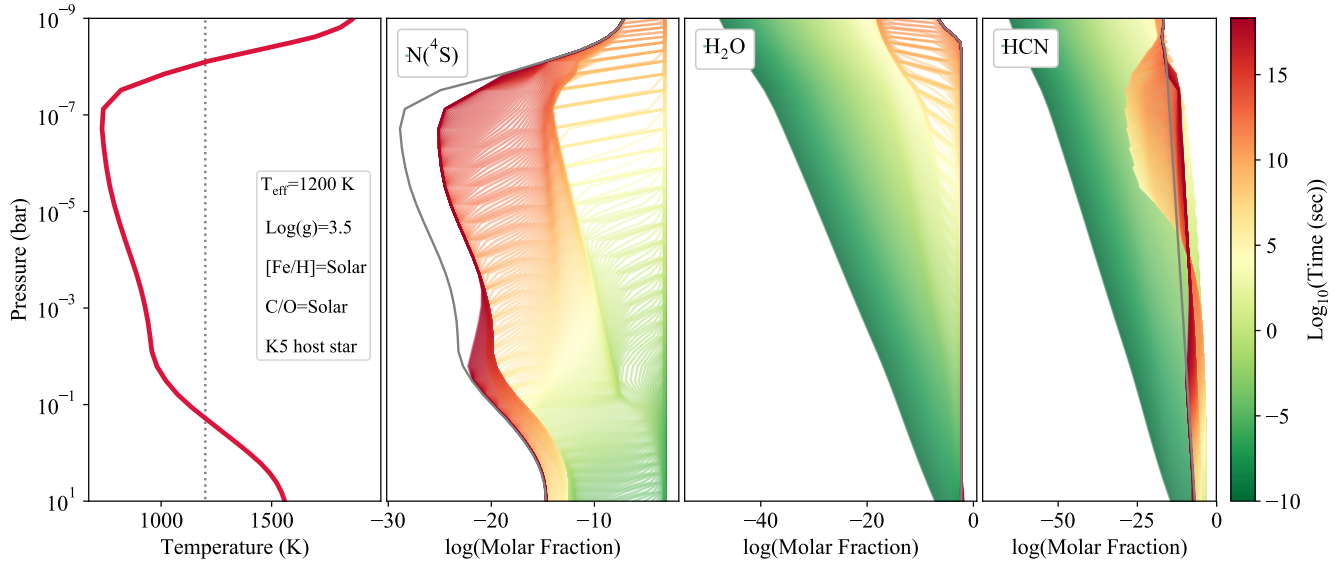


Figure 14. Similar to Figure 13 but with a 1D model; without the inclusion of vertical mixing or photolyses. **left)** Temperature profile of an irradiated exoplanet with $T_{\text{eff}}=1200$ K, $\log(g)=3.5$, with solar metallicity and C/O ratio, orbiting around a K5 star. **Rest of panels)** from left to right: The temporal evolution of $\text{N}(^4\text{S})$, H_2O , and HCN abundances, color-coded by time, where green to red shows the progress in time from 10^{-10} sec to more than the age of universe, 1.6×10^{18} sec. The thermochemically reversed model (colored lines) is in agreement with the thermochemical equilibrium calculations (gray lines) at adequately high temperatures (≥ 1000 K). However, abundances at pressures between 10^{-2} and 10^{-8} bar (< 1000 K) have not fully reached their thermochemical equilibrium yet and demand longer integration times.

reached their thermochemical equilibrium and require longer integration times. This shows that the calculation of thermochemical equilibrium is better performed through Gibbs free energy minimization.

As already mentioned, the “kinetically thermochemical equilibrium” mode, i.e. solving the system of ODEs without diffusion or photolyses, can be used as a pre-processing step to initialize the model with thermochemical equilibrium abundances. However, ChemKM has the option to quickly calculate abundances at thermochemical equilibrium by using Gibbs free energy minimization. Figure 10 shows an example of such a setup, where the model is initialized by using Gibbs free energy minimization and *all* abundances remain the same in the kinetic calculations due to the lack of additional physics such as diffusion or photolyses, hence verifying the validity of our reversible setup to reach or keep the same composition as in thermochemical equilibrium. See Section A.6 for a description of initialization options in ChemKM.

B.3. Molecular and eddy diffusion

Transport-induced quenching is one of the main kinetic-related disequilibrium processes in planetary atmospheres. Both molecular and eddy diffusion could play pivotal roles to drive away the atmospheric composition from their thermochemical equilibrium. If the chemical kinetic timescales are larger than the transport timescales, the mole fraction of a parcel of gas can become quenched in the atmosphere. This usually happens when the temperature and pressure are low enough that the kinetic reactions cannot rapidly occur in both directions; allowing the diffusion processes to drive the system away from its thermochemical equilibrium state.

Figure 15 gives an example for such a system with a 1D atmosphere evolving from its thermochemical equilibrium state. We use the same setup as our 1D example presented in the previous section (Figure 14), but initialize the composition with their thermochemical equilibrium values. We include a vertically constant eddy diffusion ($K_{zz}=10^4 \text{ cm}^2\text{s}^{-1}$) in the model. We choose this relatively low K_{zz} to demonstrate its significance even in the case of a hot atmosphere (e.g. in this case $T_{\text{eff}}=1200$ K). No photolyses is included in this setup to only present the effect of diffusion. The abundances reach to a new steady state known as the “diffusion equilibrium” (e.g. Lettau 1951). A cross-section of Figure 15 at 10^{-10} bar is shown in Figure 16 to graphically illustrate the evolution of abundances until they reach the diffusion equilibrium at TOA. Continuing the integration until 10^{20} sec did not change this new steady state within numerical errors; hence we conclude that this state is a real diffusion equilibrium.

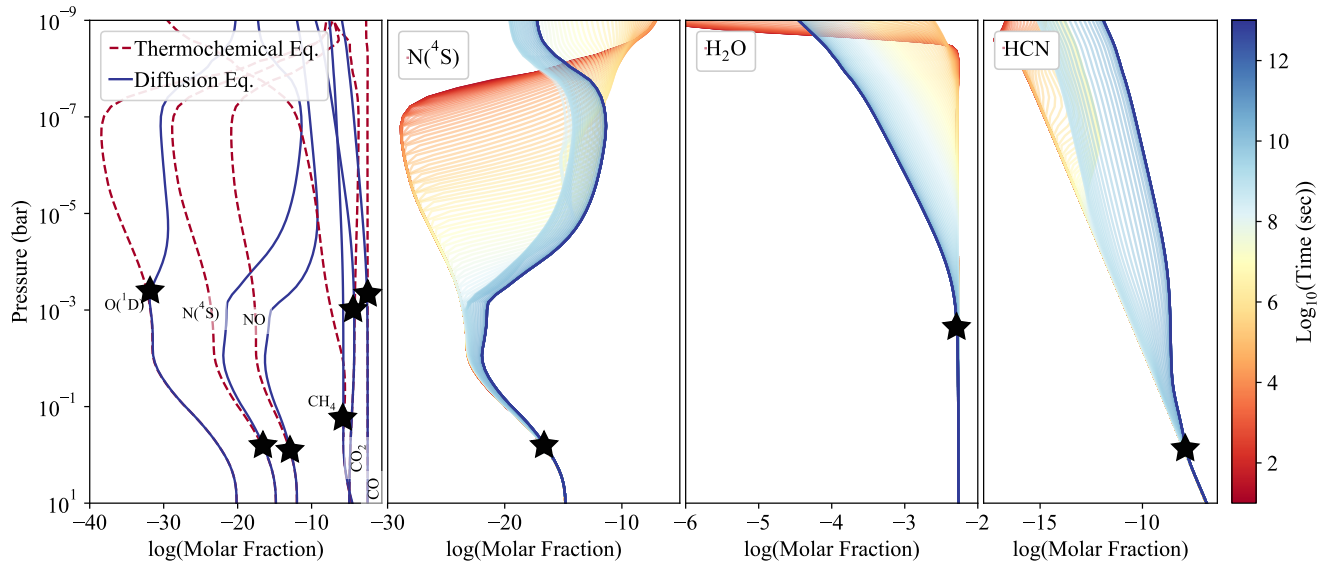


Figure 15. Time evolution of our 1D model presented in Figure 14 from its thermochemical equilibrium state to diffusion equilibrium, by introducing molecular diffusion and a vertically constant eddy diffusion ($K_{zz}=10^4 \text{ cm}^2\text{s}^{-1}$). **Left panel)** Thermochemical equilibrium (dashed red lines) and diffusion equilibrium of $\text{O}(^1\text{D})$, $\text{N}(^4\text{S})$, NO , CH_4 , CO_2 , CO (solid blue lines). **Rest of panels)** Temporal evolution of $\text{N}(^4\text{S})$, H_2O , and HCN abundances in detail. They are color-coded by time, where blue to red shows the progress in time from 10^1 sec to 10^{13} sec. The quenching points are shown by the stars.

The quenching levels of $\text{O}(^1\text{D})$, $\text{N}(^4\text{S})$, NO , CH_4 , CO_2 , CO , see Figure 15, are in agreement with the general estimations of quenching levels in Venot et al. (2018). The quenching level of each constituent, however, depends on its chemical kinetics timescales, ranging from 1 to 10^{-3} bar in this example.

A commonly used definition of the “quenching point” (a.k.a. quenching pressure or quenching level) is that the composition of all species remain constant above that level, that is the abundances remain the same as their abundances of their quenching point (e.g. Moses 2014). This assumption has been also used to mimic a parameterization of disequilibrium processes, usually in the retrieval models as a trade-off to gain more speed (e.g. Madhusudhan & Seager 2011). However, a constant abundance profile is rarely the case in realistic planetary atmospheres and atmospheric constituent abundances could show significant deviations from their quenched abundances. Prominent processes at mbar level, such as molecular diffusion or photolysis, could drive the abundance profiles away from an idealized constant profile. A non-isothermal TP structure, for example a hot thermosphere with local heating at TOA (as it is the case in the current example, see the TP structure in Figure 14), can result in a variation of chemical timescales at different altitudes and might trigger the system to move in and out of thermochemical equilibrium. Including the vertical diffusion causes mixing of these abundances at different pressures; potentially keeping them away from a constant profile. For instance, dissociation of H_2O at TOA due to a hot upper thermosphere depletes its abundances at higher pressures through vertical mixing, see Figure 15 and Figure 3.

In addition, such sharp temperature gradient could also enhance the molecular diffusion (see Equation 2), resulting in more deviation from a constant abundance profile. The left panel of Figure 15 represents such examples, where abundances do not remain constant above their quenching points (black stars) both due to molecular diffusion and thermal–dissociation. More discussion will follow in Section 3.3. As a rule of thumb, a constant quenched abundance profile is likely to be valid when the chemical kinetics timescale is much shorter than the timescale of all other processes at all pressures above the quenching point.

B.4. Photochemistry

Photochemistry is another prominent disequilibrium process in planetary atmospheres. We examine the same case as in the previous section, but include photochemistry instead of diffusion. We use an updated version of Hébrard et al. (2012) photolysis reactions (originally adapted from the MPI-Mainz UV/VIS Spectral Atlas Keller-Rudek et al. (2013)) and a stellar flux similar to the average solar flux over an entire solar cycle from Thuillier et al. (2004) as

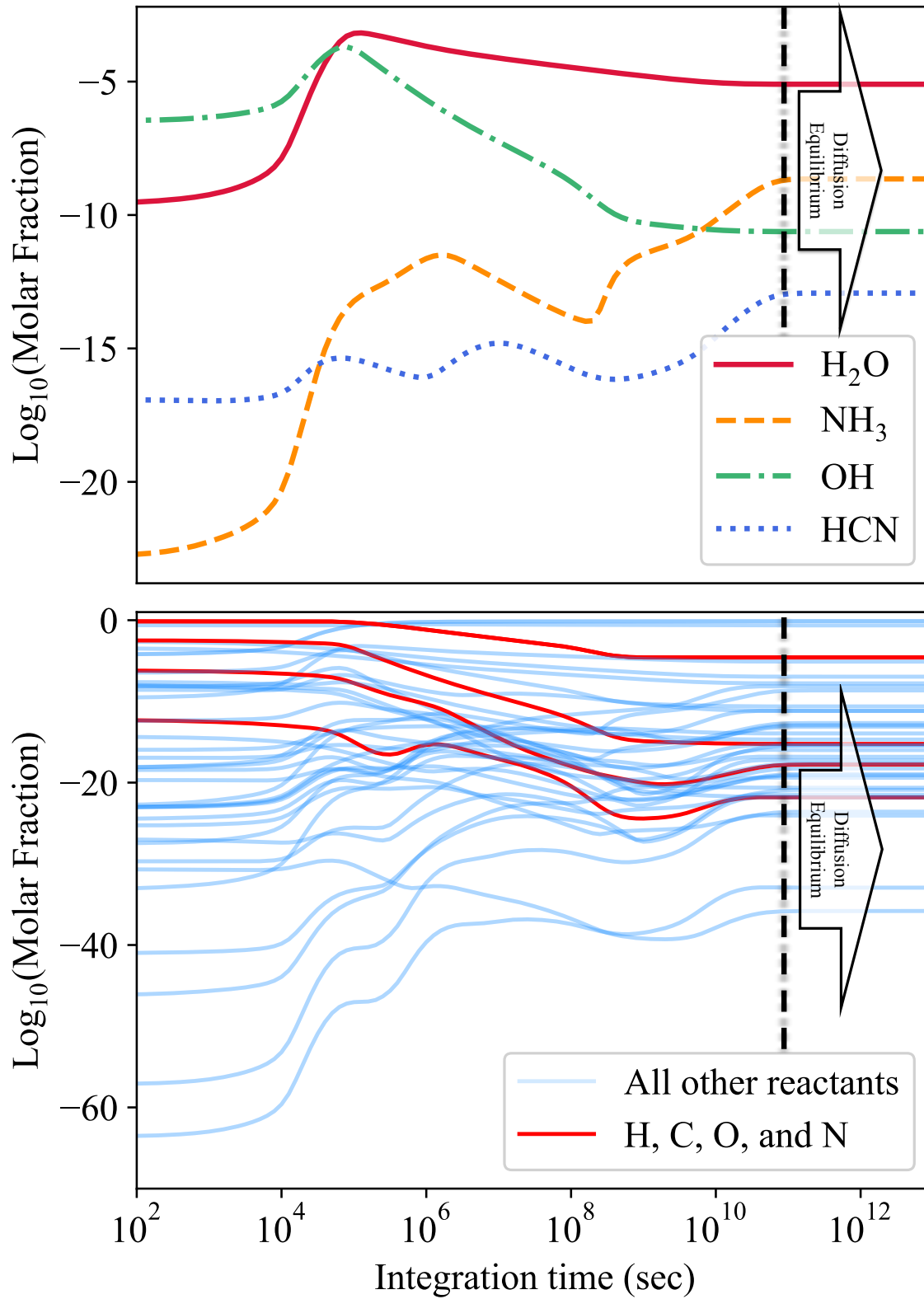


Figure 16. A cross-section of Figure 15 at 10^{-10} bar to illustrate the "diffusion-equilibrium" at the top of the atmosphere after 10^{11} sec.

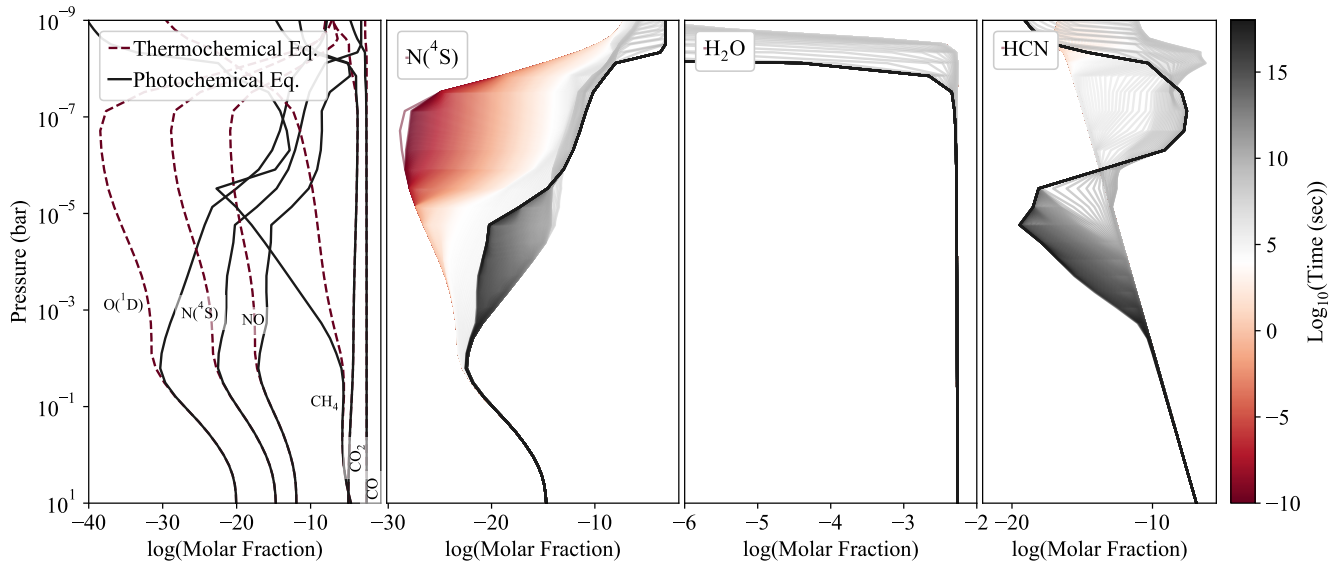


Figure 17. Temporal evolution of the 1D model presented in Figure 14 but evolving from its thermochemical equilibrium to photochemical equilibrium by introducing photolysis into the model. No diffusion is included in the model to purely present the effect of photolysis. The temporal evolution of abundances are color-coded by time, where red to black shows the progress in time from 10^{-10} sec to beyond the age of universe, 10^{18} sec. Abundances around 10^{-3} bar have not fully reached their photochemical equilibrium yet and require longer integration times.

the radiation flux at TOA. We initialize abundances with their thermochemical equilibrium values, identical to the previous section initialization.

Figure 17 shows the effect of photolysis on this model. The photochemical timescales are typically shorter than diffusion processes and hence the photolysis should be the dominant mechanism at TOA. Each species responds to the irradiation differently, depending on its shielding and UV cross-section. Some have excess production through photolysis reactions, e.g. $N(^4S)$ in this model, some face considerable destruction by this process, e.g. H_2O , and some could have a combination of those depending on the altitude, e.g. HCN .

After some time, the system reaches a new steady state, the “photochemical equilibrium”, balancing between reversible reactions and photodissociation. The required integration time to achieve photochemical equilibrium at all vertical levels strongly depends on the atmospheric temperature structure; with hotter atmospheres tending to reach the photochemical equilibrium faster. This is evident in Figure 17, where reaching the photochemical equilibrium at around 10^{-3} bar requires integration times larger than the age of the universe.

Absorption cross-sections, the quantum yields, and the actinic flux⁵ at a given altitude determine the photodissociation rate of a photo-reactant. Figure 18 shows the irradiation at TOA and the actinic flux at different pressures. The stellar flux quickly vanishes at wavelengths shorter than 220 nm due to strong UV absorption cross-section of photo-reactants at those wavelengths. The rest of the stellar flux is also affected by Rayleigh scattering in this model.

B.5. Condensation

To demonstrate ChemKM’s ability to capture condensation, we model an atmosphere with a temperature structure similar to that of Neptune. This “cold” case creates a suitable environment to examine this process, although ChemKM is capable of including the condensation for hot planets as well. No diffusion or photolysis is included in this model. We also employ the Venot (2012) kinetic network with no reverse reaction. First, we consider a nearly water-saturated atmosphere. This nearly water-saturated atmosphere would allow the condensation to begin at pressures below the intersection of Neptune’s TP structure and H_2O ’s condensation curve. We initialize the model identical to the Moses et al. (2018) Neptune model, except for He and H_2O abundances, and assume an initial atmospheric composition of 80.8% H_2O , 19% He, 1.2×10^{-3} CH_4 and 8×10^{-8} CO. The particle size is also assumed to be $0.15 \mu m$ and

⁵ “The quantity of light available to molecules at a particular point in the atmosphere and which, on absorption, drives photochemical processes in the atmosphere.” See Calvert (1990) for more details.

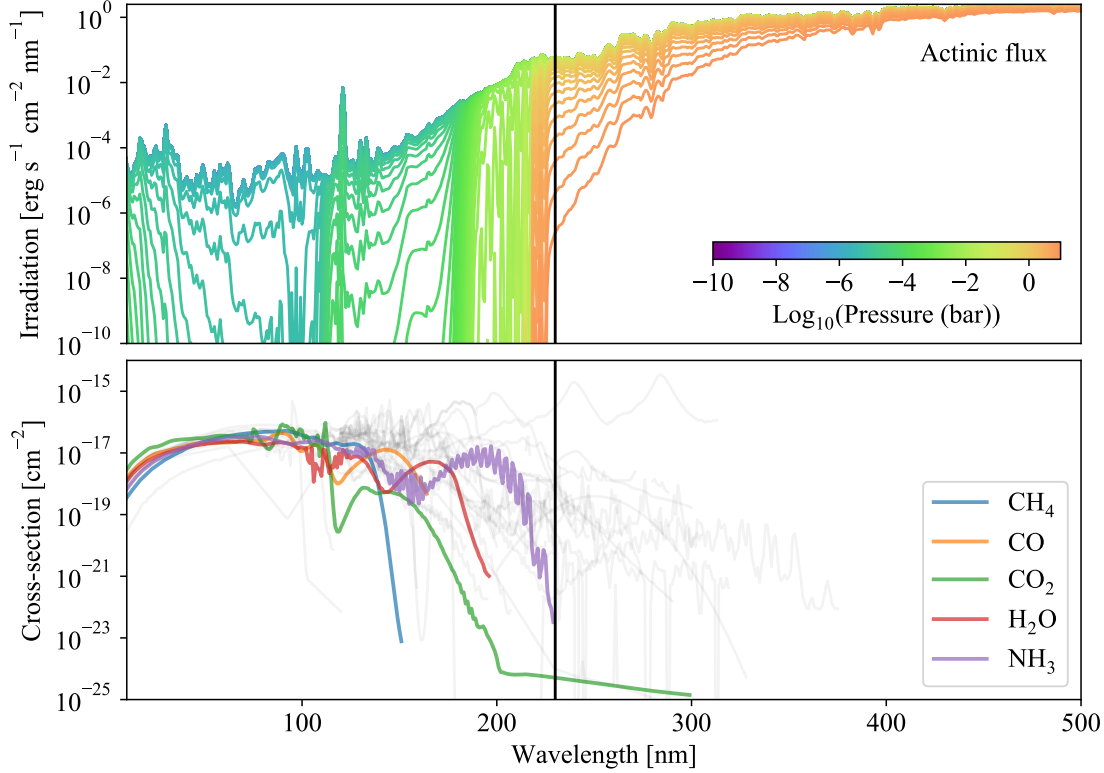


Figure 18. **Top)** Local stellar intensity (actinic flux) in logarithmic scale. Lower pressures are color-coded by cooler colors. **Bottom)** UV absorption cross-section of species in `ChemKM` (gray). Some of the species with usually major opacity contributions are shown in color.

fixed, following the Moses et al. (2018) assumption. Figure 19 shows the production of $\text{H}_2\text{O}[s]$ (water ice) under these circumstances, with the expected condensation rates discussed in Section A.3.

In reality, water condensation in the atmosphere of Neptune occurs at higher pressures (≈ 0.01 -1 bar) due to water undersaturation. However, the temperature increases again at the regions deeper than 1 bar, causing the water to remain in the gas phase and making the ≈ 0.01 -1 bar region a tropopause “cold-trap”. This is shown for water condensation in Figure 20. The initial abundances for this model are 80.8% H_2 , 19% He, and the rest is CH_4 and CO with molar fraction of 1.2×10^{-3} and 8×10^{-8} respectively, identical to the initial conditions in Moses et al. (2018). We allow for the condensation of H_2O , NO, N_2 , O_2 , C, HCN, CH_4 , CO, CO_2 , C_2H_2 , C_2H_4 , and C_2H_6 for demonstration purposes. Condensation of C_2H_2 and C are shown in Figure 20 as examples. In this setup, carbon condenses at all altitudes. However, most Neptune photochemical models do not allow carbon to condensate. This is to maintain a higher production rate of hydrocarbons, such as C_2H_2 and C_2H_6 .

B.6. Influxes and boundary conditions

Ablation, atmospheric escape, and GCR can be included in `ChemKM` by setting the influx or production rate of reagents. To demonstrate these capabilities, we use the same Neptune model and initialization as the previous section. We include molecular and eddy diffusion as well as photolysis in this case.

First, we only include an influx of H_2O equal to 2×10^5 molecules $\text{cm}^{-2}\text{s}^{-1}$ (as discussed in the Moses et al. 2018) to examine how abundances would change. We initialize the atmospheric composition by its “photo-diffusion equilibrium”⁶. We use the same K_{zz} and irradiation spectrum as in the Moses et al. (2018) Neptune model. Any deviation from this state will be caused by the imposed influx. Figure 21 shows the time evolution of H_2O , CO, $\text{O}(^1\text{D})$ and C_2H_2 abundances. As one might expect, H_2O , CO, and $\text{O}(^1\text{D})$ abundances increase, but C_2H_2 remains almost

⁶ The steady state after the inclusion of photochemistry and diffusion in the model

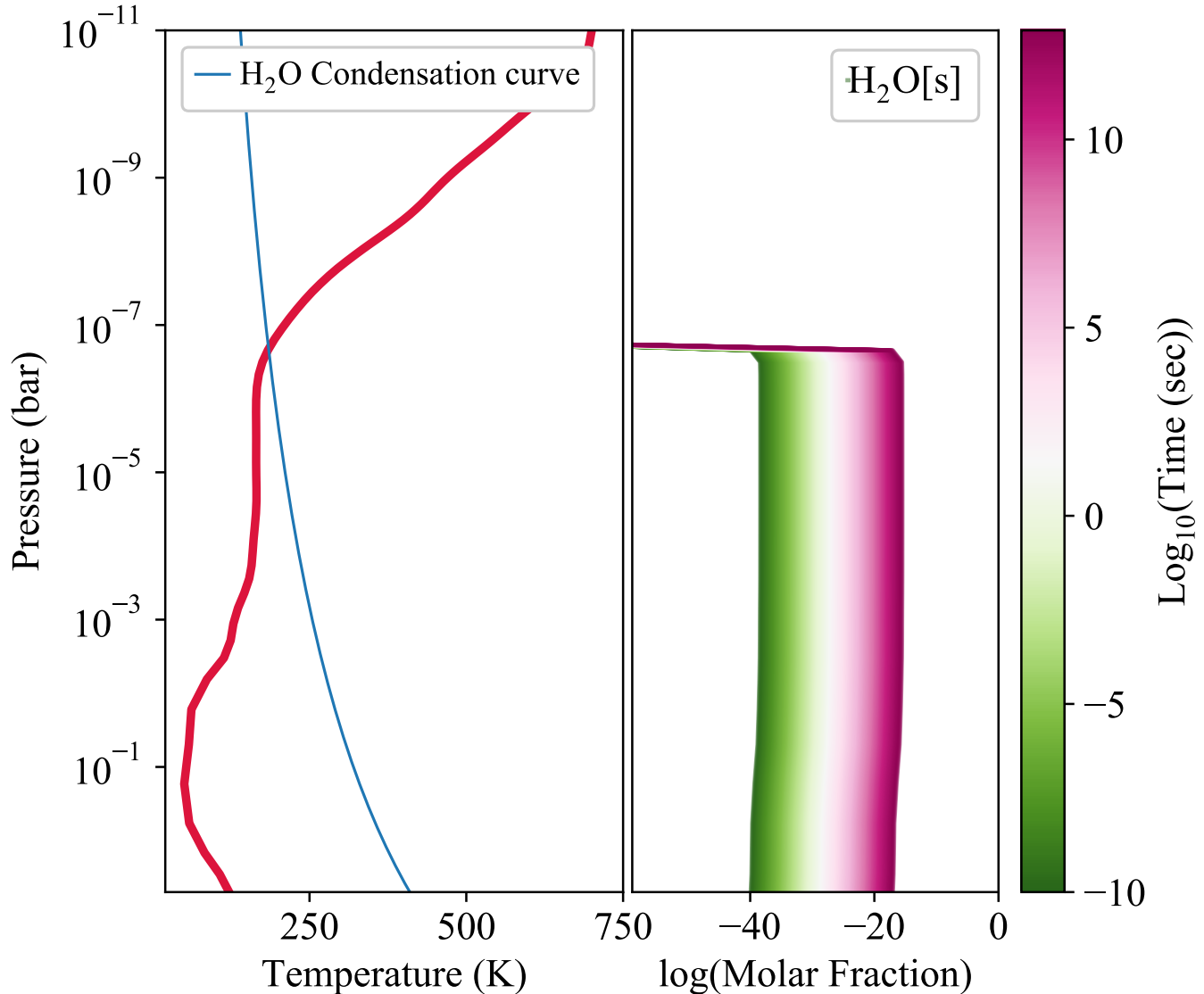


Figure 19. Water condensation in a nearly water-saturated Neptune-like planet, i.e. the temperature profile is similar to that of Neptune, but the initial composition is set to 80.8% H₂O, 19% He, and the rest is CH₄ and CO with molar fraction of 1.2×10^{-3} and 8×10^{-8} respectively. Water condensation occurs (right panel) below the intersection of the TP profile (left panel red line) and H₂O's condensation curve (left panel blue line).

the same, due to the lack of free radical carbon. Diffusion plays a pivotal role and transports the deposited material at TOA to the deeper parts of the atmosphere. In this model, the abundance variations caused by H₂O influx at 10^{-11} bar typically require 10^5 - 10^7 sec (weeks to months) to reach 10^{-7} bar, where the highest altitude measurements of hydrocarbon mixing ratios have taken place (e.g. Moses et al. 2018). This time scale would be very different if the required oxygen to explain the observations were supplied by a large cometary impact (e.g. Lellouch et al. 2005; Luszcz-Cook & de Pater 2013; Moses et al. 2018). These possibilities can be addressed by JWST measurements of Neptune's composition (e.g. Roman et al. 2018; Fletcher et al. 2018) or a dedicated mission to ice-giants (e.g. Hofstadter et al. 2017).

In the next case study, we run the same model but include an influx of 2×10^8 molecules $\text{cm}^{-2}\text{s}^{-1}$ CO (see Moses et al. 2018, for the motivation) in addition to H₂O. Under these circumstances, excessive production of free carbon radicals and therefore additional carbon-bearing compounds can be expected. However, individual species at different altitudes might respond to these free radicals differently. Photolysis of incoming H₂O and CO results in the production of free radical H, C, and O; hence an increase in the abundance of their elements is expected (e.g. see the variation

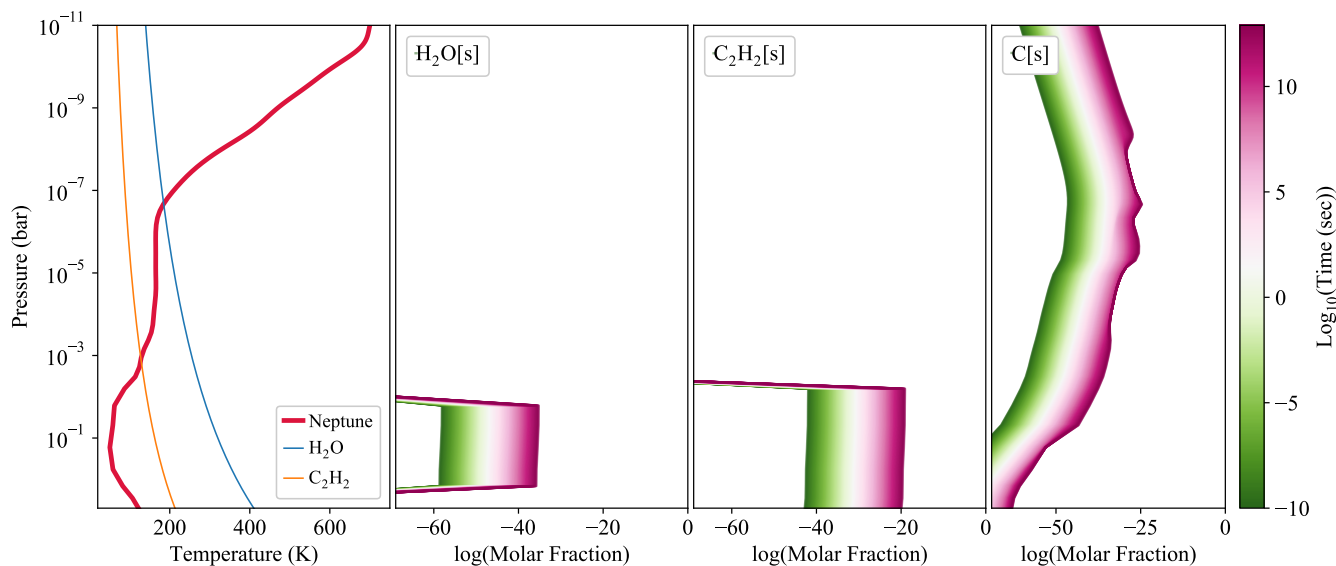


Figure 20. Condensation and cold-trap on Neptune. **Left)** Neptune’s temperature structure (red line) and condensation curves of H_2O (blue line) and C_2H_2 (orange line). **Rest of panels)** Temporal evolution of condensate production, and formation of a cold-trap roughly between 1 and 0.01 bar.

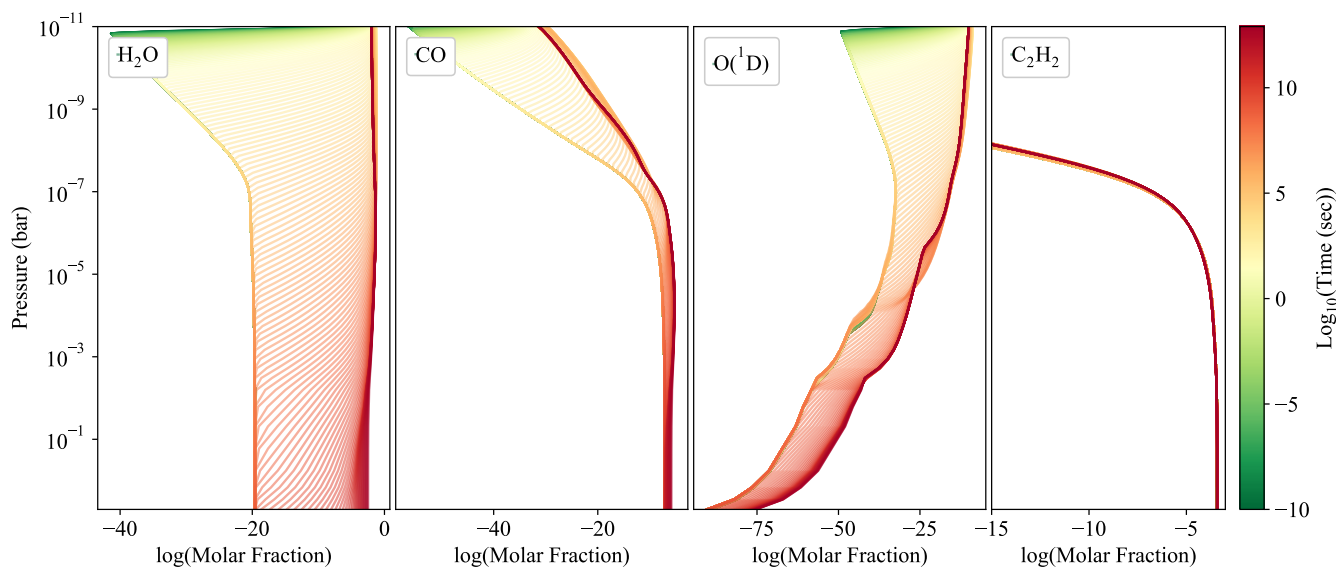


Figure 21. Abundance variations due to $2 \times 10^5 \text{ molecules cm}^{-2}\text{s}^{-1}$ water influx at TOA. The model has a temperature structure similar to the Neptune model presented in Figure 20, but we initialize the atmospheric composition by its “photo-diffusion equilibrium”; to study the abundance deviations only due to the water-influx.

of $\text{O}(^1\text{D})$ abundances in Figure 22), unless there are sink terms with higher loss rates. As expected, the production of CO and C_2H_2 are enhanced early in the simulation, however, at later times ($t \gtrsim 10^6 \text{ sec}$), C_2H_2 abundances seem to be restored to their initial values. This is, of course, not a universal trend and an examination of C_2H_2 abundance reveals its depletion at pressures between 0.1 and 10^{-7} bar. Although CO photodissociation enhances C_2H_2 production by offering additional free carbons, it also shields it at longer timescales and returns the C_2H_2 abundances at TOA to their initial values. This extra shielding also causes the depletion of C_2H_2 at mid-pressures and depletion of H_2O and $\text{O}(^1\text{D})$ abundances at TOA.

Similar to these models, boundaries with fixed molar fractions and vertical profile of influxes of reagents (i.e. production rates) can be easily included in ChemKM’s modeling setup. In the case of GCRs, ChemKM includes a separated

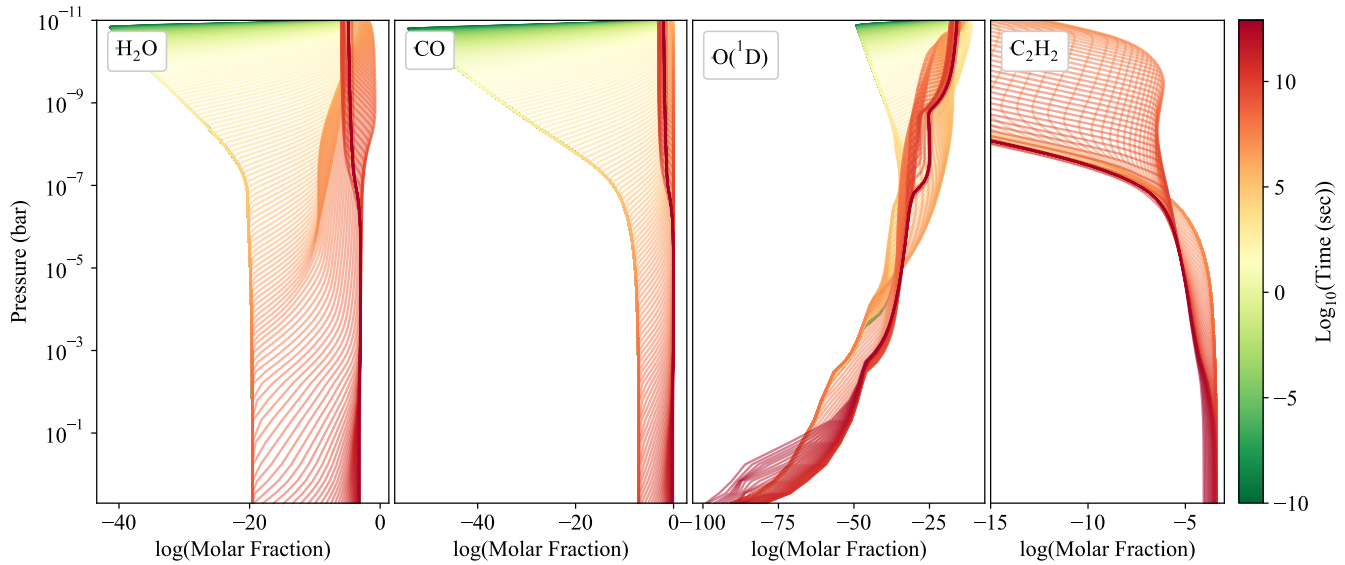


Figure 22. Similar to Figure 21 but additionally 2×10^8 molecules $\text{cm}^{-2}\text{s}^{-1}$ CO influx is included.

module to take into account the effect of Galactic/solar cosmic rays. Vertical profiles of production rates of each species with their branching and yields for each GCR reaction can be provided in the current version of the code (similar to the setup of photolysis module).

REFERENCES

- Agúndez, M., Venot, O., Iro, N., et al. 2012, *Astronomy & Astrophysics*, 548, A73. <https://www.aanda.org/articles/aa/abs/2012/12/aa20365-12/aa20365-12.html>
- Allen, M., Yung, Y. L., & Waters, J. W. 1981, *Journal of Geophysical Research: Space Physics*, 86, 3617
- Alonso-Floriano, F. J., Sánchez-López, A., Snellen, I. a. G., et al. 2019, *Astronomy & Astrophysics*, 621, A74. <https://articles/aa/abs/2019/01/aa34339-18/aa34339-18.html>
- Aplin, K. L., & Harrison, R. G. 2016, *Nature Communications*, 7, 11976. <https://www.nature.com/articles/ncomms11976>
- Atreya, S. K., Wong, M. H., Owen, T. C., et al. 1999, *Planetary and Space Science*, 47, 1243. <http://www.sciencedirect.com/science/article/pii/S0032063399000471>
- Bazilevskaya, G. 2000, *Space Science Reviews*, 94, 25. <https://doi.org/10.1023/A:1026721912992>
- Bishop, J., Romani, P. N., & Atreya, S. K. 1998, *Planetary and Space Science*, 46, 1. <http://www.sciencedirect.com/science/article/pii/S0032063397001268>
- Blumenthal, S. D., Mandell, A. M., Hébrard, E., et al. 2018, *The Astrophysical Journal*, 853, 138. <https://doi.org/10.3847/2F1538-4357/2Faa9e51>
- Brain, D. A., McFadden, J. P., Halekas, J. S., et al. 2015, *Geophysical Research Letters*, 9142. <https://agupubs.onlinelibrary.wiley.com/doi/abs/10.1002/2015GL065293%4010.1002/%28ISSN%291944-8007.MAVEN1>
- Brogi, M., Giacobbe, P., Guilluy, G., et al. 2018, *Astronomy & Astrophysics*, 615, A16. <https://articles/aa/abs/2018/07/aa32189-17/aa32189-17.html>
- Brogi, M., Kok, R. J. d., Albrecht, S., et al. 2016, *The Astrophysical Journal*, 817, 106. <https://doi.org/10.3847/2F0004-637x%2F817%2F2%2F106>
- Burrows, A., & Sharp, C. M. 1999, *The Astrophysical Journal*, 512, 843. <http://iopscience.iop.org/article/10.1086/306811/meta>
- Calvert, J. G. 1990, *Pure and Applied Chemistry*, 62, 2167. <https://www.degruyter.com/view/j/pac.1990.62.issue-11/pac199062112167/pac199062112167.xml>
- Capone, L. A., Dubach, J., Prasad, S. S., & Whitten, R. C. 1983, *Icarus*, 55, 73. <http://www.sciencedirect.com/science/article/pii/0019103583900519>
- Changeat, Q., Edwards, B., Waldmann, I., & Tinetti, G. 2019, arXiv:1903.11180 [astro-ph], arXiv: 1903.11180. <http://arxiv.org/abs/1903.11180>

- Clancy, R. T., & Sandor, B. J. 1998, *Geophysical Research Letters*, 25, 489. <https://agupubs.onlinelibrary.wiley.com/doi/abs/10.1029/98GL00114>
- Danielson, R. E. S. 1968, APR. 1-2, 1966. <https://ntrs.nasa.gov/search.jsp?R=19680063391>
- Divine, N. 1974, Titan atmosphere models, 1973. [Saturn satellite], Tech. rep. <https://ntrs.nasa.gov/search.jsp?R=19740008423>
- Divine, N. P. 1972, SEE N72-31964 22-34, p. p 1. <https://ntrs.nasa.gov/search.jsp?R=19720024315>
- Dobrijevic, M., Cavalié, T., Hébrard, E., et al. 2010, *Planetary and Space Science*, 58, 1555. <http://www.sciencedirect.com/science/article/pii/S0032063310002266>
- Dobrijevic, M., Hébrard, E., Loison, J. C., & Hickson, K. M. 2014, *Icarus*, 228, 324. <http://www.sciencedirect.com/science/article/pii/S001910351300434X>
- Drummond, B., Tremblin, P., Baraffe, I., et al. 2016, *Astronomy & Astrophysics*, 594, A69. <https://www.aanda.org/articles/aa/abs/2016/10/aa28799-16/aa28799-16.html>
- Encrenaz, T. H. 1974, Observational constraints on model atmospheres for Uranus and Neptune. <https://ntrs.nasa.gov/search.jsp?R=19750037243>
- Fletcher, L., Encrenaz, T., Orton, G., Moses, J., & Rowe-Gurney, N. 2018, in , B5.4–4–18. <http://adsabs.harvard.edu/abs/2018cosp...42E1077F>
- Fortney, J. J., Marley, M. S., Lodders, K., Saumon, D., & Freedman, R. 2005, *The Astrophysical Journal Letters*, 627, L69. <http://iopscience.iop.org/article/10.1086/431952/meta>
- France, K., Loyd, R. O. P., Youngblood, A., et al. 2016, *The Astrophysical Journal*, 820, 89. <https://doi.org/10.3847/2F0004-637x%2F820%2F2%2F89>
- Gao, P., Fan, S., Wong, M. L., et al. 2017, *Icarus*, 287, 116. <http://www.sciencedirect.com/science/article/pii/S0019103516306170>
- Gilbert, R. G., Luther, K., & Troe, J. 1983, *Berichte der Bunsengesellschaft für physikalische Chemie*, 87, 169. <https://onlinelibrary.wiley.com/doi/abs/10.1002/bbpc.19830870218>
- Gladstone, G. R., Stern, S. A., Ennico, K., et al. 2016, *Science*, 351, aad8866. <https://science.sciencemag.org/content/351/6279/aad8866>
- Greene, T. P., Line, M. R., Montero, C., et al. 2016, *The Astrophysical Journal*, 817, 17. <https://doi.org/10.3847/2F0004-637x%2F817%2F1%2F17>
- Guilluy, G., Sozzetti, A., Brogi, M., et al. 2019, arXiv:1904.04170 [astro-ph], arXiv: 1904.04170. <http://arxiv.org/abs/1904.04170>
- Hawkes, R. L., Milley, E. P., Ehrman, J. M., et al. 2008, in *Advances in Meteoroid and Meteor Science*, ed. J. M. Trigo-Rodríguez, F. J. M. Rietmeijer, J. Llorca, & D. Janches (New York, NY: Springer New York), 331–336. https://doi.org/10.1007/978-0-387-78419-9_47
- Haynes, W. M. 2016, *CRC Handbook of Chemistry and Physics*, 97th edn. (CRC Press), google-Books-ID: bNDMBQAAQBAJ
- Helling, C. 2019, *Annual Review of Earth and Planetary Sciences*, 47, null. <https://doi.org/10.1146/annurev-earth-053018-060401>
- Helling, C., Gourbin, P., Woitke, P., & Parmentier, V. 2019, arXiv:1901.08640 [astro-ph], arXiv: 1901.08640. <http://arxiv.org/abs/1901.08640>
- Helling, C., Jardine, M., & Mokler, F. 2011, *The Astrophysical Journal*, 737, 38. <https://doi.org/10.1088%2F0004-637x%2F737%2F1%2F38>
- Helling, C., & Rimmer, P. B. 2019, arXiv:1903.04565 [astro-ph, physics:physics], doi:10.1098/rsta.2018.0398, arXiv: 1903.04565. <http://arxiv.org/abs/1903.04565>
- Hindmarsh, A. C. 1983, *Scientific Computing*, 1, 55. <https://computation.llnl.gov/casc/nsde/pubs/u88007.pdf>
- Hofstadter, m., Simon, A., Reth, K., & Elliot, J. 2017, *Ice Giants Mission Planning*, NASA Mission Study JPL D-100520, Solar System Exploration Directorate Jet Propulsion Laboratory. https://www.lpi.usra.edu/icegiants/mission_study/
- Hu, R., & Seager, S. 2014, *The Astrophysical Journal*, 784, 63. <https://doi.org/10.1088%2F0004-637x%2F784%2F1%2F63>
- Hu, R., Seager, S., & Bains, W. 2012, *The Astrophysical Journal*, 761, 166. <https://doi.org/10.1088%2F0004-637x%2F761%2F2%2F166>
- . 2013, *The Astrophysical Journal*, 769, 6. <https://doi.org/10.1088%2F0004-637x%2F769%2F1%2F6>
- Hubeny, I. 2017, *Monthly Notices of the Royal Astronomical Society*, 469, 841
- Hunten, D. M. 1982, *Planetary and Space Science*, 30, 773. <http://www.sciencedirect.com/science/article/pii/S0032063382901106>
- Hébrard, E., Dobrijevic, M., Loison, J. C., Bergeat, A., & Hickson, K. M. 2012, *Astronomy & Astrophysics*, 541, A21. <https://www.aanda.org/articles/aa/abs/2012/05/aa18837-12/aa18837-12.html>
- Hébrard, E., Dobrijevic, M., Loison, J. C., et al. 2013, *Astronomy & Astrophysics*, 552, A132. <https://www.aanda.org/articles/aa/abs/2013/04/aa20686-12/aa20686-12.html>

- Hörst, S. M., Vuitton, V., & Yelle, R. V. 2008, *Journal of Geophysical Research: Planets*, 113, doi:10.1029/2008JE003135. <https://agupubs.onlinelibrary.wiley.com/doi/abs/10.1029/2008JE003135>
- Irwin, P. G. J., Toledo, D., Garland, R., et al. 2018, *Nature Astronomy*, 2, 420. <https://www.nature.com/articles/s41550-018-0432-1>
- . 2019, *Icarus*, 321, 550. <http://www.sciencedirect.com/science/article/pii/S0019103518306109>
- Jakosky, B. M., Grebowsky, J. M., Luhmann, J. G., & Brain, D. A. 2015, *Geophysical Research Letters*, 42, 8791. <https://agupubs.onlinelibrary.wiley.com/doi/abs/10.1002/2015GL065271>
- Jasper, A. W., Klippenstein, S. J., Harding, L. B., & Ruscic, B. 2007, *The Journal of Physical Chemistry A*, 111, 3932. <https://doi.org/10.1021/jp067585p>
- Keating, D., & Cowan, N. B. 2018, arXiv:1809.00002 [astro-ph], arXiv: 1809.00002. <http://arxiv.org/abs/1809.00002>
- Kee, R. J., Rupley, F., & Miller, M. 1989, Sandia National Laboratories Report. <https://ci.nii.ac.jp/naid/10017172558/>
- Keller-Rudek, H., Moortgat, G. K., Sander, R., & Sørensen, R. 2013, *Earth System Science Data*, 5, 365. <https://www.earth-syst-sci-data.net/5/365/2013/>
- Kreidberg, L., Bean, J. L., Désert, J.-M., et al. 2014, *Nature*, 505, 69. <https://www.nature.com/articles/nature12888>
- Lavvas, P., Griffith, C. A., & Yelle, R. V. 2011, *Icarus*, 215, 732. <http://www.sciencedirect.com/science/article/pii/S0019103511002582>
- Lellouch, E., Moreno, R., & Paubert, G. 2005, *Astronomy & Astrophysics*, 430, L37. <https://www.aanda.org/articles/aa/abs/2005/05/aagk052/aagk052.html>
- Lellouch, E., Romani, P. N., & Rosenqvist, J. 1994, *Icarus*, 108, 112. <http://www.sciencedirect.com/science/article/pii/S0019103584710451>
- Lettau, H. 1951, in *Compendium of Meteorology: Prepared under the Direction of the Committee on the Compendium of Meteorology*, ed. H. R. Byers, H. E. Landsberg, H. Wexler, B. Haurwitz, A. F. Spilhaus, H. C. Willett, H. G. Houghton, & T. F. Malone (Boston, MA: American Meteorological Society), 320–333. https://doi.org/10.1007/978-1-940033-70-9_27
- Line, M. R., Vasisht, G., Chen, P., Angerhausen, D., & Yung, Y. L. 2011, *The Astrophysical Journal*, 738, 32. <https://doi.org/10.1088%2F0004-637x%2F738%2F1%2F32>
- Line, M. R., Marley, M. S., Liu, M. C., et al. 2017, *The Astrophysical Journal*, 848, 83. <http://stacks.iop.org/0004-637X/848/i=2/a=83>
- Lodders, K., & Fegley, B. 2002, *Icarus*, 155, 393. <http://www.sciencedirect.com/science/article/pii/S0019103501967405>
- . 2006, in *Astrophysics Update 2*, ed. J. W. Mason, Springer Praxis Books (Berlin, Heidelberg: Springer Berlin Heidelberg), 1–28. https://doi.org/10.1007/3-540-30313-8_1
- Lou, G. Y. 1973, Models of earth's atmosphere (90 to 2500 km), Tech. rep. <https://ntrs.nasa.gov/search.jsp?R=19730018598>
- Luszcz-Cook, S. H., & de Pater, I. 2013, *Icarus*, 222, 379. <http://www.sciencedirect.com/science/article/pii/S0019103512004484>
- Madhusudhan, N. 2012, *The Astrophysical Journal*, 758, 36
- Madhusudhan, N., & Seager, S. 2009, *The Astrophysical Journal*, 707, 24. <https://doi.org/10.1088%2F0004-637x%2F707%2F1%2F24>
- . 2011, *The Astrophysical Journal*, 729, 41. <http://stacks.iop.org/0004-637X/729/i=1/a=41>
- Marley, M. S., Seager, S., Saumon, D., et al. 2002, *The Astrophysical Journal*, 568, 335. <https://doi.org/10.1086%2F338800>
- Mayor, M., & Queloz, D. 1995, *Nature*, 378, 355. <https://www.nature.com/articles/378355a0>
- McBride, B. J., Zehe, M. J., & Gordon, S. 2002, NASA Glenn Coefficients for Calculating Thermodynamic Properties of Individual Species, Technical Paper E-13336, NASA, National Aeronautics and Space Administration John H. Glenn Research Center at Lewis Field Cleveland, Ohio 44135-3191. <https://www.grc.nasa.gov/WWW/CEAWeb/TP-2002-21556.htm>
- Miguel, Y., & Kaltenegger, L. 2014, *The Astrophysical Journal*, 780, 166. <http://stacks.iop.org/0004-637X/780/i=2/a=166>
- Miguel, Y., Kaltenegger, L., Linsky, J. L., & Rugheimer, S. 2014, *Monthly Notices of the Royal Astronomical Society*, 446, 345
- Molaverdikhani, K., Henning, T., & Mollière, P. 2019, *The Astrophysical Journal*, 873, 32. <https://doi.org/10.3847%2F1538-4357%2Faafda8>
- Molaverdikhani, K., McGouldrick, K., & Esposito, L. W. 2012, *Icarus*, 217, 648
- Molina-Cuberos, G. J., López-Moreno, J. J., Rodrigo, R., Lara, L. M., & O'Brien, K. 1999, *Planetary and Space Science*, 47, 1347. <http://www.sciencedirect.com/science/article/pii/S0032063399000562>

- Mollière, P., Boekel, R. v., Bouwman, J., et al. 2017, *Astronomy & Astrophysics*, 600, A10. <https://www.aanda.org/articles/aa/abs/2017/04/aa29800-16/aa29800-16.html>
- Mollière, P., van Boekel, R., Dullemond, C., Henning, T., & Mordasini, C. 2015, *The Astrophysical Journal*, 813, 47
- Mollière, P., Wardenier, J. P., van Boekel, R., et al. 2019, arXiv:1904.11504 [astro-ph], arXiv: 1904.11504. <http://arxiv.org/abs/1904.11504>
- Morley, C. V., Fortney, J. J., Marley, M. S., et al. 2012, *The Astrophysical Journal*, 756, 172. <https://doi.org/10.1088%2F0004-637x%2F756%2F2%2F172>
- Moses, J. I. 1991, phd, California Institute of Technology. <http://resolver.caltech.edu/CaltechETD:etd-08012006-093137>
- . 1992, *Icarus*, 99, 368. <http://www.sciencedirect.com/science/article/pii/001910359290153X>
- . 2014, *Phil. Trans. R. Soc. A*, 372, 20130073. <http://rsta.royalsocietypublishing.org/content/372/2014/20130073>
- Moses, J. I., Bézard, B., Lellouch, E., et al. 2000a, *Icarus*, 143, 244. <http://www.sciencedirect.com/science/article/pii/S001910359996270X>
- Moses, J. I., Fletcher, L. N., Greathouse, T. K., Orton, G. S., & Hue, V. 2018, *Icarus*, 307, 124. <http://www.sciencedirect.com/science/article/pii/S0019103517307935>
- Moses, J. I., Lellouch, E., Bézard, B., et al. 2000b, *Icarus*, 145, 166. <http://www.sciencedirect.com/science/article/pii/S0019103599963200>
- Moses, J. I., & Poppe, A. R. 2017, *Icarus*, 297, 33. <http://www.sciencedirect.com/science/article/pii/S001910351730180X>
- Moses, J. I., Visscher, C., Fortney, J. J., et al. 2011, *The Astrophysical Journal*, 737, 15. <https://doi.org/10.1088%2F0004-637x%2F737%2F1%2F15>
- Nejad, L. A. M. 2005, *Astrophysics and Space Science*, 299, 1. <https://doi.org/10.1007/s10509-005-2100-z>
- Niemann, H. B., Atreya, S. K., Carignan, G. R., et al. 1998, *Journal of Geophysical Research: Planets*, 103, 22831. <https://agupubs.onlinelibrary.wiley.com/doi/abs/10.1029/98JE01050>
- Noll, K. S., Geballe, T. R., Leggett, S. K., & Marley, M. S. 2000, *The Astrophysical Journal*, 541, L75. <https://doi.org/10.1086%2F312906>
- Noll, R., & McElroy, M. 1972, *Models of Venus atmosphere (1972)*, Tech. rep. <https://ntrs.nasa.gov/search.jsp?R=19730008097>
- . 1974, *Models of Mars' atmosphere (1974)*, Tech. rep. <https://ntrs.nasa.gov/search.jsp?R=19750011035>
- Parmentier, V., Showman, A. P., & Lian, Y. 2013, *Astronomy & Astrophysics*, 558, A91. <https://www.aanda.org/articles/aa/abs/2013/10/aa21132-13/aa21132-13.html>
- Pater, I. d., Sault, R. J., Butler, B., DeBoer, D., & Wong, M. H. 2016, *Science*, 352, 1198. <https://science.sciencemag.org/content/352/6290/1198>
- Pearce, B. K. D., Ayers, P. W., & Pudritz, R. E. 2019, *The Journal of Physical Chemistry A*, doi:10.1021/acs.jpca.8b11323. <https://doi.org/10.1021/acs.jpca.8b11323>
- Pino, L., Ehrenreich, D., Wyttenbach, A., et al. 2018, *Astronomy & Astrophysics*, 612, A53. <https://articles/aa/abs/2018/04/aa31244-17/aa31244-17.html>
- Poling, B., Prausnitz, J., & Connell, J. O. 2000, *The Properties of Gases and Liquids (McGraw Hill Professional)*, google-Books-ID: E920LnqY2woC
- Rimmer, P. B., & Helling, C. 2013, *The Astrophysical Journal*, 774, 108. <https://doi.org/10.1088%2F0004-637x%2F774%2F2%2F108>
- Roman, M. T., Fletcher, L. N., Banfield, D. J., & Gierasch, P. J. 2018, *AGU Fall Meeting Abstracts*, 31. <http://adsabs.harvard.edu/abs/2018AGUFM.P31B..05R>
- Rossow, W. B. 1978, *Icarus*, 36, 1. <http://www.sciencedirect.com/science/article/pii/0019103578900726>
- Salz, M., Czesla, S., Schneider, P. C., & Schmitt, J. H. M. M. 2016, *Astronomy & Astrophysics*, 586, A75. <https://www.aanda.org/articles/aa/abs/2016/02/aa26109-15/aa26109-15.html>
- Saumon, D., Marley, M. S., Lodders, K., & Freedman, R. S. 2003, *Symposium - International Astronomical Union*, 211, 345. <https://www.cambridge.org/core/journals/symposium-international-astronomical-union/article/nonequilibrium-chemistry-in-the-atmospheres-of-brown-dwarfs/F67F0F6158934EEBC200D46AE2BF8AF8>
- Scheucher, M., Grenfell, J. L., Wunderlich, F., et al. 2018, *The Astrophysical Journal*, 863, 6, arXiv: 1808.02347. <http://arxiv.org/abs/1808.02347>
- Schiff, M. H., Jaffe, J. S., & Freundlich, B. 2014, *Annals of the Rheumatic Diseases*, 73, 1549. <https://www.ncbi.nlm.nih.gov/pmc/articles/PMC4112421/>
- Seager, S., Liang, M.-C., Parkinson, C. D., & Yung, Y. L. 2005, *Proceedings of the International Astronomical Union*, 1, 491. <https://www.cambridge.org/core/journals/proceedings-of-the-international-astronomical-union/article/exoplanet-atmospheres-and-photochemistry/4D397F3F9D7C839FEE02A2F61A39B0CE>

- Seinfeld, J. H. 1986, Atmospheric chemistry and physics of air pollution (Wiley), google-Books-ID: NAhSAAAAMAAJ
- Seinfeld, J. H., & Pandis, S. N. 2012, Atmospheric Chemistry and Physics: From Air Pollution to Climate Change (John Wiley & Sons), google-Books-ID: YH2K9eWsZOcC
- Selesnick, R. S., & Stone, E. C. 1991, Geophysical Research Letters, 18, 361. <https://agupubs.onlinelibrary.wiley.com/doi/abs/10.1029/90GL02582>
- Sing, D. K., Fortney, J. J., Nikolov, N., et al. 2016, Nature, 529, 59
- Skemer, A. J., Hinz, P. M., Esposito, S., et al. 2012, The Astrophysical Journal, 753, 14. <https://doi.org/10.1088%2F0004-637x%2F753%2F1%2F14>
- Stevenson, K. B., Harrington, J., Nymeyer, S., et al. 2010, Nature, 464, 1161. <https://www.nature.com/articles/nature09013>
- Stewart, P. H., Larson, C. W., & Golden, D. M. 1989, Combustion and Flame, 75, 25. <http://www.sciencedirect.com/science/article/pii/0010218089900849>
- Stokes, R. J., & Evans, D. F. 1997, Fundamentals of Interfacial Engineering (John Wiley & Sons), google-Books-ID: QuEeGZpj9kC
- Strobel, D. F., Meier, R. R., Summers, M. E., & Strickland, D. J. 1991, Geophysical Research Letters, 18, 689. <https://agupubs.onlinelibrary.wiley.com/doi/abs/10.1029/91GL00133>
- Stubenrauch, C. J., Rossow, W. B., Kinne, S., et al. 2013, Bulletin of the American Meteorological Society, 94, 1031. <https://journals.ametsoc.org/doi/full/10.1175/BAMS-D-12-00117.1>
- Thuillier, G., Floyd, L., Woods, T. N., et al. 2004, Advances in Space Research, 34, 256. <http://www.sciencedirect.com/science/article/pii/S0273117704002388>
- Troe, J. 1983, Berichte der Bunsengesellschaft für physikalische Chemie, 87, 161. <https://onlinelibrary.wiley.com/doi/abs/10.1002/bbpc.19830870217>
- Tsai, S.-M., Lyons, J. R., Grosheintz, L., et al. 2017, The Astrophysical Journal Supplement Series, 228, 20. <https://doi.org/10.3847%2F1538-4365%2F228%2F2%2F20>
- Velinov, P. 1968, Journal of Atmospheric and Terrestrial Physics, 30, 1891. <http://www.sciencedirect.com/science/article/pii/0021916968900317>
- Venot, O. 2012, thesis, Bordeaux 1. <http://www.theses.fr/2012BOR14610>
- Venot, O., Bounaceur, R., Dobrijevic, M., et al. 2019, arXiv:1902.04939 [astro-ph], arXiv: 1902.04939. <http://arxiv.org/abs/1902.04939>
- Venot, O., Drummond, B., Miguel, Y., et al. 2018, Experimental Astronomy, 46, 101. <https://doi.org/10.1007/s10686-018-9597-y>
- Venot, O., Hébrard, E., Agúndez, M., Decin, L., & Bounaceur, R. 2015, Astronomy & Astrophysics, 577, A33. <https://www.aanda.org/articles/aa/abs/2015/05/aa25311-14/aa25311-14.html>
- Venot, O., Hébrard, E., Agúndez, M., et al. 2012, Astronomy & Astrophysics, 546, A43. <https://www.aanda.org/articles/aa/abs/2012/10/aa19310-12/aa19310-12.html>
- Vuitton, V., Yelle, R. V., Lavvas, P., & Klippenstein, S. J. 2011, The Astrophysical Journal, 744, 11. <https://doi.org/10.1088%2F0004-637x%2F744%2F1%2F11>
- Wang, D., Miguel, Y., & Lunine, J. 2017, The Astrophysical Journal, 850, 199. <https://doi.org/10.3847%2F1538-4357%2Faa978e>
- West, R. A. 2017, Nature, 551, 302. <https://www.nature.com/articles/551302a>
- West, R. A., Baines, K. H., Karkoschka, E., & Sánchez-Lavega, A. 2009, in Saturn from Cassini-Huygens, ed. M. K. Dougherty, L. W. Esposito, & S. M. Krimigis (Dordrecht: Springer Netherlands), 161–179. https://doi.org/10.1007/978-1-4020-9217-6_7
- Yung, Y. L., Allen, M., & Pinto, J. P. 1984, Astrophysical Journal Supplement Series, 55, 465. <http://resolver.caltech.edu/CaltechAUTHORS:20140909-090508298>
- Zahnle, K. J., & Marley, M. S. 2014, The Astrophysical Journal, 797, 41. <http://stacks.iop.org/0004-637X/797/i=1/a=41>
- Zalesky, J. A., Line, M. R., Schneider, A. C., & Patience, J. 2019, arXiv:1903.11658 [astro-ph], arXiv: 1903.11658. <http://arxiv.org/abs/1903.11658>
- Zhang, X., & Showman, A. P. 2018, arXiv:1808.05365 [astro-ph], arXiv: 1808.05365. <http://arxiv.org/abs/1808.05365>